In situ commissioning of the ATLAS electromagnetic calorimeter with cosmic muons

M. Cooke[a], P.S. Mangeard[b], M. Plamondon[c]

M. Aleksa[d], M. Delmastro[d], L. Fayard[c], S. Henrot-Versille[c], F. Hubaut[b], R. Lafaye[e], W. Lampl[f], J. Leveque[b], H. Ma[g], E. Monnier[b], J. Parsons[a], P. Pralavorio[b], Ph. Schwemling[h], L. Serin[c], B. Trocme[i], G. Unal[d], M. Vincter[j], H. Wilkens[d]

[a] *Columbia University, Nevis Laboratory, 136 So. Broadway, Irvington, NY 10533, United States of America*
[b] *CPPM, Aix-Marseille Université, CNRS/IN2P3, Marseille, France*
[c] *LAL, Univ. Paris-Sud, IN2P3/CNRS, Orsay, France*
[d] *CERN, CH-1211 Genève 23, Switzerland*
[e] *Laboratoire dAnnecy-le-Vieux de Physique des Particules LAPP, IN2P3/CNRS, Université de Savoie, France*
[f] *University of Arizona, Department of Physics, Tucson, AZ 85721, United States of America*
[g] *Brookhaven National Laboratory, Physics Department, Bldg. 510A, Upton, NY 11973, United States of America*
[h] *Laboratoire de Physique Nucléaire et de Hautes Energies, Université Pierre et Marie Curie (Paris 6), Université Denis Diderot (Paris-7), IN2P3-CNRS, Tour 33, 4 place Jussieu, FR - 75252 Paris Cedex 05, France*
[i] *Laboratoire de Physique Subatomique et de Cosmologie, CNRS-IN2P3, Université Joseph Fourier, INPG, 53 avenue des Martyrs, FR - 38026 Grenoble Cedex, France*
[j] *Carleton University, Department of Physics, 1125 Colonel By Drive, Ottawa ON K1S 5B6, Canada*

ATL-LARG-PUB-2007-013
15 December 2007

Abstract

In 2006, ATLAS entered the *in situ* commissioning phase. The primary goal of this phase is to verify the detector operation and performance with cosmic muons. Using a dedicated cosmic muon trigger from the hadronic Tile calorimeter, a sample of approximately 120000 events was collected in several modules of the barrel electromagnetic (EM) calorimeter between August 2006 and March 2007. As cosmic events are generally non-projective and arrive asynchronously with respect to the trigger clock, methods to improve the standard signal reconstruction for this situation are presented. Various selection criteria for projective muons and clustering algorithms have been tested, leading to preliminary results on calorimeter uniformity in η and timing performance.

Contents

1 Introduction

All ATLAS sub-detectors are presently in the last stage of installation in the cavern at Point 1 of the LHC accelerator. After installation and connection to the services, extensive testing must be performed. The first phase of commissioning verifies the proper functioning of the detectors in stand-alone mode. In the next phase, the different sub-detectors are integrated into the common data acquisition, monitoring, detector control and safety system frameworks. The process of integrating more and more sub-systems is ongoing since summer 2006 when the first common partition between the Liquid Argon (LAr) barrel electromagnetic (EM) calorimeter and the hadronic Tile barrel calorimeter was created.

Analyzing cosmic muon events is the only way to test the EM calorimeter *in situ* with physics signals before LHC collisions. In order to trigger on cosmic muon events, special programmable coincidence boards have been produced (see section 2) that use the LVL1 output of the Tile calorimeter trigger towers. Simulations show that a few cosmic muons per minute are expected to pass close to the interaction point. Pseudo-projective[1] events are therefore expected in the EM calorimeter. Noise reduction and signal reconstruction are challenges for the muon signal extraction, as cosmic muons arrive asynchronously and usually deposit only several hundred MeV when passing through the EM calorimeter. However, it was shown in test beam analyses [1, 2] that a muon signal can be extracted in the second sampling with a signal to noise ratio greater than 7 over the full detector coverage. As will be demonstrated in this note, the ratio can be further increased to approximately twice this value when using a longer part of the signal pulse shape for the amplitude reconstruction than that foreseen in high rate LHC running.[2]

As a result of the continuing installation phase in the ATLAS cavern, cosmic run conditions have not been stable. For this note, which demonstrates the potential of the cosmic muon analysis, a set of runs taken in August and October 2006 and one in March 2007 have been chosen for detailed study. However, cosmic muon data collection has continued while this note was in preparation (summer and fall of 2007) and will continue until the start of the LHC.

The note is organized as follows. A general description of the barrel EM and Tile calorimeters is given in section 2, along with a description of the dedicated cosmic trigger and the conditions during the data collection. The procedures to reconstruct the muon signal in the EM calorimeter are discussed in section 3, as well as studies of the muon trajectory and arrival time correlation between EM and Tile. An initial scan for dead cells is made along with observations of physics signals in a region at non-nominal high voltage. These results are presented in section 4. Despite the limited size of the sample, section 5 provides an initial assessment of the calorimeter performance. Concluding remarks are given in section 6.

[1] Here and in the following, a cosmic muon trajectory is called projective if the particle passes within several centimeters of the interaction point (IP). A pseudo-projective trajectory is one where the muon passes within several tens of centimeters of the IP. A more quantitative definition is given later in the note.

[2] For LHC running, 5 digital samples (one every 25 ns) will be read out from the front end electronics and will be used to reconstruct the signal amplitude. For the cosmic runs considered in this note, 32 samples were read out.

2 Cosmic muon data collection

The ATLAS barrel calorimeter (EM & Tile) was installed in its final position in the Point 1 cavern in October 2005. After installation of the services, the barrel cryostat was cooled and the EM calorimeter filled with liquid argon in the summer of 2006. Since then cosmic muon runs have been taken. Brief descriptions of the EM and hadronic parts of the barrel calorimeter are given in sections 2.1 and 2.2, respectively. Since the ATLAS muon trigger was not yet available at the time of data taking, a dedicated trigger, described in section 2.3, was instrumented to trigger on cosmic muons. Finally, the conditions during the data collection periods are discussed in section 2.4.

2.1 Electromagnetic Calorimeter

The EM calorimeter is a LAr sampling calorimeter and the barrel section covers the range $|\eta| < 1.475$. The barrel is composed of 2 wheels separated at $\eta = 0$, with side A covering $\eta > 0$ and side C $\eta < 0$. Each wheel consists of 16 modules divided in three samplings in depth whose granularities in ϕ and η are given in Table 1 and Figure 1.[3] An important quantity for cosmic muon studies is the depth of EM calorimeter cells. As demonstrated in Appendix 1, cosmic muons can be considered minimum ionizing particles (MIPs) and thus their energy deposition is proportional to the length of the active sampling traversed. Therefore the depth of cells is a major factor in determining the overall calorimeter response to muons. The depth as a function of η is shown in Figure 2 [4]. In this figure, the depth is quoted in terms of radiation lengths. However, the energy deposition of MIPs correlates better with the product of the length and density of the material.

2.2 Hadronic Tile Calorimeter

The hadronic barrel calorimeter is a sampling calorimeter with iron absorbers and scintillating tiles as the active material. It is composed of 3 parts, one central ($|\eta| < 1.0$) and two extended ($0.8 < |\eta| < 1.7$). Each part is divided in 64 modules in ϕ, segmented in 3 compartments in depth. The central part (LBA and LBC) is located around the cryostat of the EM barrel calorimeter. The granularities of the different samplings, less fine than the EM calorimeter, are also summarized in Table 1.

Module	η range	Sampling 1 (S1)	Sampling 2 (S2)	Sampling 3 (S3)
EM Barrel	0 to 1.35	0.003×0.1	0.025×0.025	0.05×0.025
	1.35 to 1.4	0.025×0.1	0.025×0.025	-
	1.4 to 1.475	0.025×0.1	0.075×0.025	-
Tile Barrel	0 to 1.6	0.1×0.1	0.1×0.1	0.2×0.1

Table 1: Granularity of the Barrel Calorimeter ($\Delta\eta \times \Delta\phi$)

[3] Detailed information about the design and the construction of the EM barrel calorimeter can be found in Ref. [3].

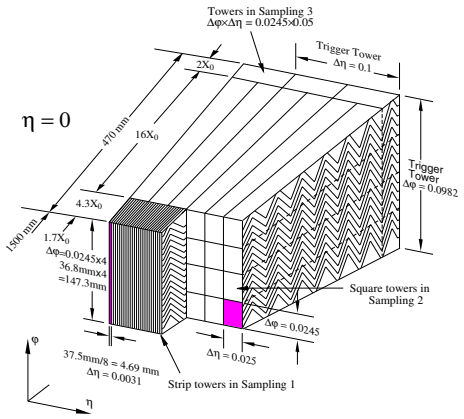

Figure 1: *Sketch of the accordion and sampling structure of the EM Calorimeter.*

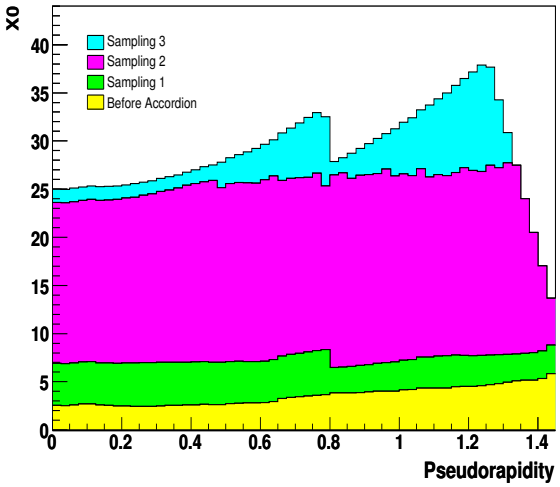

Figure 2: *Variation with pseudorapidity (η) of the sampling depth (in radiation lengths) in the barrel calorimeter. The yellow part represents the cryostat and tracker.*

2.3 Dedicated trigger for cosmic muons

A dedicated trigger using only Tile calorimeter signals was configured to detect cosmic muons. The available Tile towers [4] were included in the trigger for each data taking period. In 2006, the Tile coverage was limited to a few vertical ϕ modules on the top of side C (LBC-top in Figure 3) and the bottom of side A (LBA-bottom in Figure 3). This setup was modified in March 2007 and increased the coverage (top LBA and LBC, bottom LBA and LBC). As the η coverage of the central part of the Tile is limited to $|\eta| < 0.8$, cosmic muon analyses are restricted to this area.

Figure 3 demonstrates the logic of the trigger decision using the coincidence boards [5]. The LVL1 output of the Tile is a sum of all the analog photo multiplier outputs in low gain. As the muon signals are also small in the Tile, noise is a challenge. The thresholds must be carefully tuned tower by tower, and are roughly 1 GeV. Trigger towers which were excessively noisy were masked in order to avoid high trigger rates. In the offline analysis, it was determined that $\sim 50\%$ of the triggered events were potential cosmic events (i.e. contained a Tile cluster on the top and bottom with an energy consistent with that depositied by a muon).

2.4 Conditions of data collection

Data collection began in August 2006, continued for one full week in October 2006, and then resumed in March 2007. Since the spring of 2007 data are taken nearly every weekend. A summary of the cosmic runs used for the analyses described in this note is given in Table 2, along with the modules which were read out. The module numbering is provided in Figure 4 for the two sides of the EM barrel calorimeter.

[4] One trigger tower is the sum of all Tile cells in a region of $\Delta\eta \times \Delta\phi = 0.1 \times 0.1$.

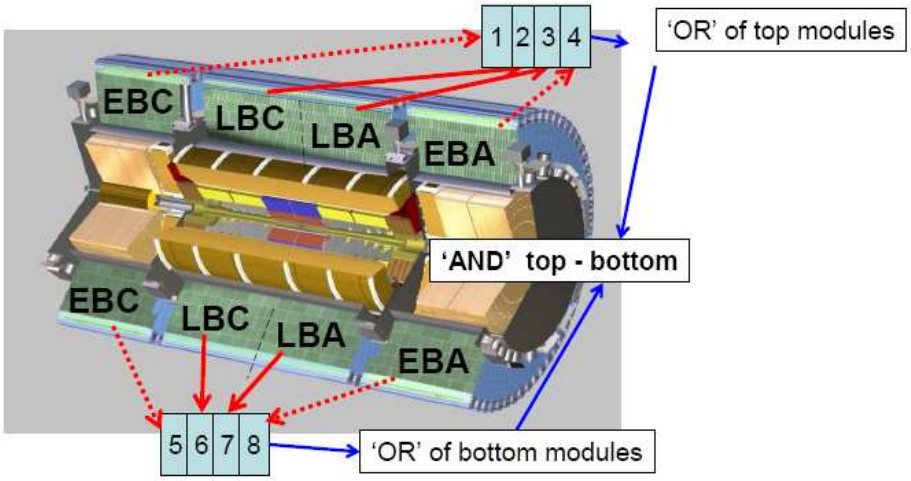

Figure 3: *Trigger setup. In 2006, only LBC modules ($\eta < 0$) were included in the top trigger, and only LBA modules ($\eta > 0$) in the bottom. For the March 2007 run considered in this note, top and bottom modules from both LBA and LBC were used. Soon after, runs were taken with the modules from the full system, including the extended barrels (EBA and EBC).*

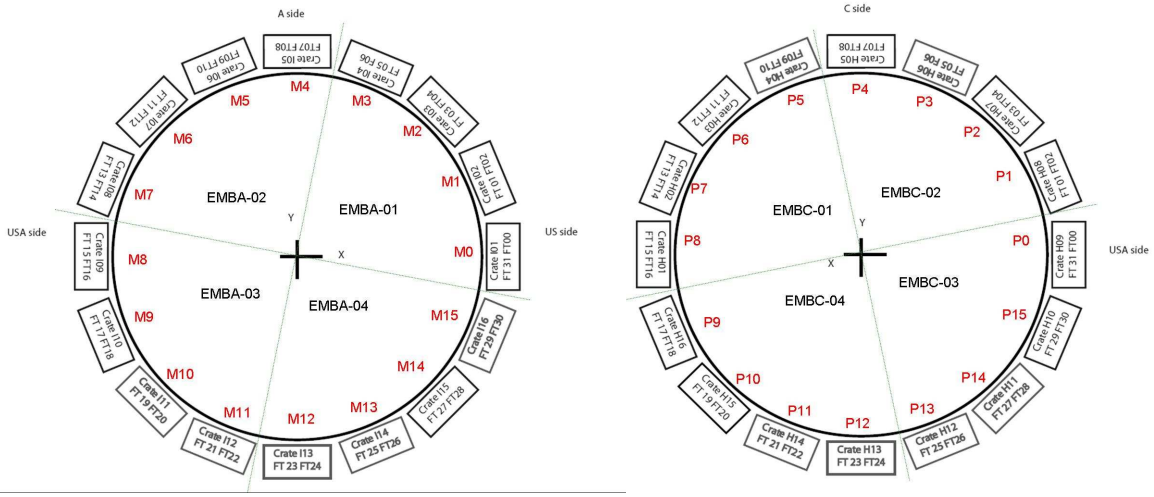

Figure 4: *The sketch depicts the two ends of the EM barrel calorimeter (each looking toward the interaction point). The boxes on the outside represent front end crates (the names are given inside the boxes). A front end crate receives the signals from one calorimeter module (names are given in red, e.g. P5), each through two feedthroughs (FT).*

Date	Run #	LAr modules (Figure 4)	LAr HV (kV)	Tile Trigger (Figure 3)	Events ($\times 10^3$)
08/2006	7810-7814	M12	2.0	LBC-top, LBA-bottom	13
10/2006	8035, 8037, 8051 8055, 8077	M11, M12 P4*, P5	1.6		78
03/2007	2060	M3, M4, M5 M11, M12 P3**,P4*, P5 P11, P12	1.6	LBC+LBA-top, LBC+LBA-bottom	28

Table 2: *Summary of run characteristics for the three periods of data taking. *FT07 of this module excluded in detailed analyses. **Module excluded in detailed analyses.*

An important difference between run periods is the trigger configuration. The trigger thresholds were set higher in March 2007 than in 2006. Additionally, the fraction of non-projective triggers increased as a result of the trigger logic and using both A and C side trigger towers on the top and bottom. The majority of the pseudo-projective events in this note come from the 2006 data.

Another difference between run periods is the high voltage (HV) applied to the EM calorimeter. In the August runs the nominal 2000 V was used whereas after, to better protect the detector from unstable conditions in the cavern, the value was lowered to 1600 V. Additionally, the applied current usually stays near a few μA. However, a small fraction of the HV zones draw a higher current. These zones are allowed to operate with higher current and the actual HV level is chosen such that the dissipated power inside the LAr bath stays below 1W. In the modules used during the cosmic data taking periods considered, only one HV zone showed a higher current and was operated at 600V. The response in this sector will be discussed in section 4.2. Lastly, each HV zone consists of two half-gaps that are individually powered with HV. Due to a HV cabling error in half of the module P4, and in P3, only one half gap was powered in these sectors. Consequently, one expects a reduced response in this region. The observation of this lower than expected response during the cosmic analysis helped elucidate this cabling error. For the detailed studies presented in this note, the regions at 600V and with reduced response are excluded.

3 Muon sample extraction

This section describes the methods used to extract a high quality sample of cosmic muon events in the EM calorimeter. First, an algorithm to reconstruct the muon trajectory and arrival time using the Tile Calorimeter is presented. The Tile information is used repeatedly in this note to compare with the results of the EM Calorimeter analysis. Next, procedures used to reconstruct the energy and time of the signal from EM calorimeter cells are described. A comparison of several cluster methods, each sensitive to different systematic effects, follows. Lastly, the consistency of the trajectory and time measurements from the EM and Tile Calorimeters is studied.

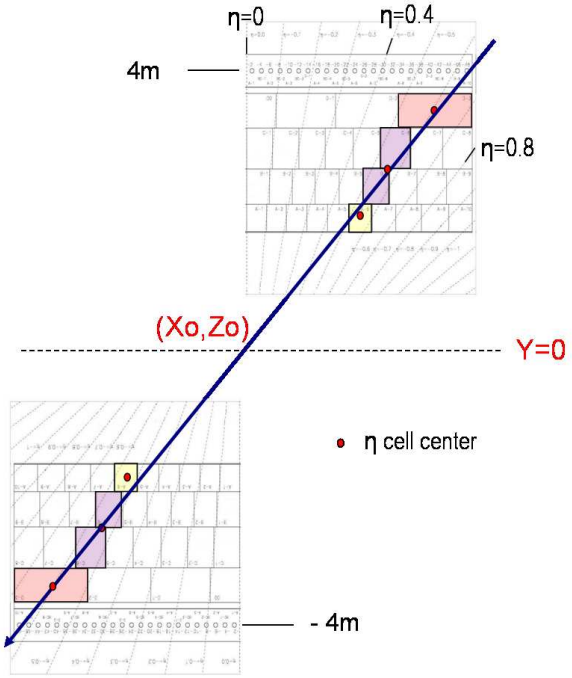

Figure 5: *Schematic depiction of a reconstructed track with the TileMuonFitter algorithm. Colored cells have energy above a threshold and red dots are their barycenters. The arrow represents the track of the muon extroplated from dots.* (X_0, Z_0) *are the coordinates of the crosspoint between the track and the horizontal plan at* $Y = 0$.

3.1 Muon reconstruction with the Tile Calorimeter

A dedicated algorithm, TileMuonFitter [6], has been developed to reconstruct cosmic muon trajectories and provide the time at the crossing of the $Y = 0$ plane (Figure 5). The trajectory is extracted by fitting with a straight line the position of Tile cells with $E_{cell} > 100$ MeV weighted by their energy density. Cells in both the top and bottom are required. To specify the fitted trajectory, the algorithm returns (X_0, Z_0), the coordinates in the $Y = 0$ plane, and a unit vector representing the direction. One simple projectivity definition used often in this note is a selection on (X_0, Z_0) (e.g. $X_0 < \pm 30$ cm and $Z_0 < \pm 30$ cm). The time is measured in each cell, and extrapolated to $Y = 0$ plane taking into account the time of flight. The timing information is then obtained by an energy weighted average.

3.2 Muon signal reconstruction with the EM Calorimeter

To obtain a high quality sample of reconstructed cosmic muons with the EM Calorimeter, the full noise reduction capability of the signal reconstruction method is utilized. Additionally, the standard procedure for reconstructing the amplitude and time must be adapted to account for the asynchronous muon arrival time.

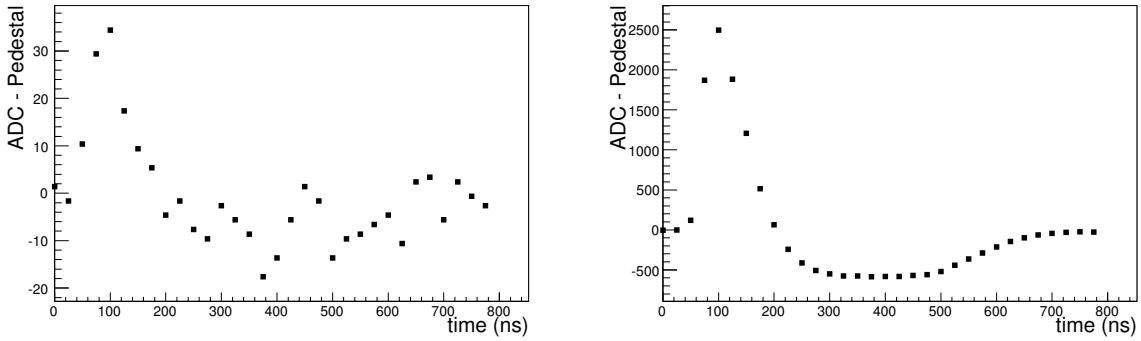

(a) (b)

Figure 6: *a) A typical signal shape from an ionizing energy deposition by a muon (∼300 MeV). b) A typical signal shape from a catastrophic energy loss of a cosmic muon (∼23 GeV). In both cases, the cell is from the second sampling and pedestals have been subtracted.*

3.2.1 Electronic noise

Figure 6a shows a typical signal shape induced by a cosmic muon with a peak around 30 ADC counts. The shape is significantly distorted by the noise which is several ADC counts. For comparison, the typical shape of a catastrophic energy loss of a cosmic muon is presented in Figure 6b.

In order to improve the signal to noise for the cosmic analysis, the noise autocorrelation between samples and an optimal filtering technique (OF) [7] are used to reconstruct the amplitude of the response shape. In the OF method, the maximum amplitude (A_{max}) and difference between the assumed and reconstructed time (Δt) are expressed as linear combinations of the samples (S_i are in ADC units, after pedestal substraction):

$$A_{max} = \sum_{k=1}^{N_s} a_k S_k \tag{1}$$

$$A_{max}\Delta t = \sum_{k=1}^{N_s} b_k S_k. \tag{2}$$

The variables a_k and b_k are sets of optimal filtering coefficients (OFCs). Figure 7 shows the noise reduction for first and second sampling cells as a function of the number of samples, N_s, used. The decrease in noise comes from two contributions. One contribution results from obtaining more signal with more samples. An additional contribution is achieved by accounting for the noise correlation between samples. In order to illustrate only the former contribution, the later one has been removed by computing OFCs which assume no noise correlation. As observed in Figure 7, a large reduction in the noise is achieved quickly until $N_s \sim 5$. A plateau is reached around $N_s \sim 10$, when the added samples contain no signal information. Further reduction is obtained when samples containing undershoot information are added. Including the noise autocorrelation reduces the noise up to $N_s \sim 7$, which corresponds to the region where the

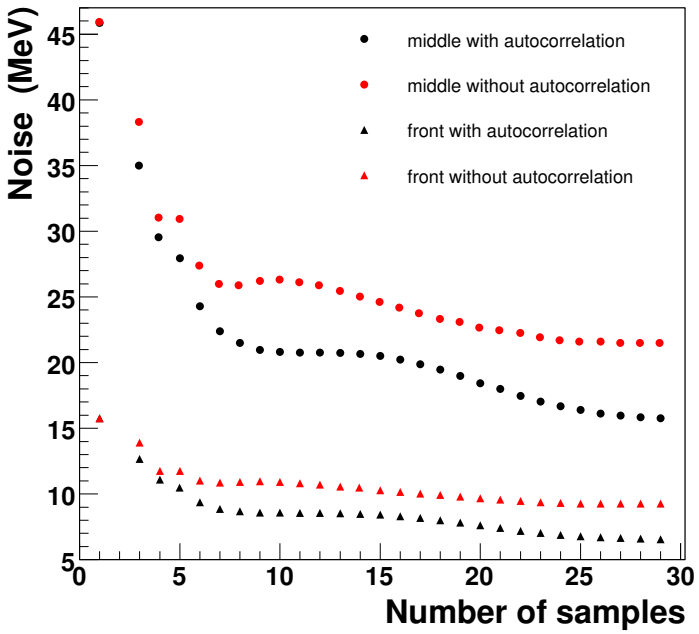

Figure 7: *The noise reduction of first (front) and second (middle) sampling cells with optimal filtering coefficients computed with and without the autocorrelation function.*

autocorrelation function is non-zero. Beyond this region, the noise reduction remains roughly parallel to that given with just increasing signal.

With 29 samples, and OFCs computed with autocorrelation information, the noise in the second sampling is reduced by a factor of $\sim$1.8 ($\sim$2.9) with respect to 5 samples (single sample). For the first sampling, the respective numbers are $\sim$1.8 ($\sim$2.6). Consequently, 29 samples are chosen in the following to reconstruct the amplitude.[5]

3.2.2 Energy and time reconstruction

In addition to the challenge of improving the signal to noise, another difficulty in the muon signal reconstruction is the asynchronous arrival time of the cosmic muons with respect to the trigger clock. In order to account for the variable start time of the waveform, the variables a_k and b_k have been computed with different phase delays in bins of 1 ns.

Several methods of OFC phase determination have been investigated. The method used in this note depends on the cluster considered (the different cluster methods will be described in detail in section 3.3). The iteration technique for phase selection is common to all cluster methods. Using Equation (2), the OFC phase choice is determined by iterating over different phases until the criterion $\Delta t < 1$ ns is satisfied. The time returned in the previous iteration is used to determine the subsequent phase choice in the next iteration.

The final phase which is converged upon is used in the time measurement. The EM cell

[5]Because of the latency settings of the read-out in calibration, a few samples before the waveform peak are digitizing the pedestal. As those samples are not used for the signal reconstruction, 29 instead of 32 sample OFCs are used.

time is defined as the waveform start time, which is ~ 50 ns before the waveform peak time.[6] The zero of the EM cell time is referenced to a default sample which is chosen to be the closest to the start of the waveform, determined by averaging over many waveforms.[7]

For the LArMuID and 3x3 clusters (section 3.3), only cells with energy above 150 MeV use iteration. A fixed phase is applied to cells below the 150 MeV threshold.[8] In contrast, for the 1x3 cluster, the phase which is determined by iteration on the maximum energy cell in the cluster is used for the other cells in the cluster. This method is referred to as $iter_{max}$. Another option for phase selection is to use the time from TileMuonFitter (section 3.1), corrected for time of flight and front end board offsets (see section 5.2.1). This method has the potential to be the most accurate. However, as explained in section 5.2.1, the Tile timing uniformity and resolution achieved during this analysis limits the performance of this method.

A detailed comparison of the methods has been performed. The study assesses the difference in phase selection as an impact on the energy of 3x3 and 1x3 clusters using the $iter_{max}$ method as a reference. Table 3 summarizes the results. In summary, all methods agree at the level of 1% with a dispersion between 1-4%.[9]

Once the amplitude has been determined, the energy of each cell is then computed as [8]:

$$E = F_{gain} \times \frac{1}{F_{I/E}} \times A_{max} \tag{3}$$

where F_{gain} is the gain of the electronics and $F_{I/E}$ is the absolute energy scale. To merge the data from August and October/March periods, where different HV values were set (section 2.4), a factor, detailed in Appendix 2, is applied. Additionally, as the drift time is a function of the HV, different sets of OFCs have been computed for each period.

3.2.3 Pulse shape analysis

The next issue involves the quality of the pulse shape prediction. A poor description of the pulse shape could result in biases when computing the OFCs and is of particular concern when a large number of samples is used. A comparison of two different methods to predict the pulse shape [9, 10] showed deviations at the 1-2% level on the shape itself or on the Mphys/Mcal factor (this factor is defined in [9]). In the following the difference between the two pulse prediction methods is neglected. The OFCs for one method have been computed for different number of samples and applied to the highest energy cell of the muon cluster (to reduce the sensitivity to cross talk). Table 4 summarizes the observed biases from the pulse prediction residuals. The largest biases come from two regions of the pulse, illustrated in Figure 8a, where the description of the shape is known to be inaccurate. Between the 5$^{\text{th}}$ and 7$^{\text{th}}$ sample, the reflection of the

[6] Depending on cosmic run conditions (trigger and LVL1 latency), the waveform peak position has moved around within the 32 samples. However, for the August/October 2006 and March 2007 runs considered here, the peak position was near the third and fourth sample respectively.

[7] In practice, the sample to which the first OFC is applied is most often the default sample. However, the iteration algorithm allows a jump to a different set of samples if necessary for convergence. The EM cell time is therefore the final phase in addition to the time associated with any jump relative to the default sample.

[8] The fixed phase is chosen to account for the average position of the peak within samples, and optimized to yield the maximum amplitude.

[9] It should be noted that not only is the r.m.s larger for the 3x3 cluster case using $iter_{>150MeV}$ $fixed_{<150MeV}$, but the distribution also exhibited some tails.

Method	Cluster 1x3		Cluster 3x3	
	bias (%)	r.m.s. (%)	bias (%)	r.m.s. (%)
$iter_{max}+4\ ns$	-0.19	0.69	-0.18	1.25
$iter_{max}-4\ ns$	-0.11	1.20	-0.12	1.78
$iter_{>150MeV}\ fixed_{<150MeV}$	-0.54	2.85	-0.51	3.56
TileMuonFitter	-0.47	2.02	-0.38	2.77

Table 3: *Energy difference (bias) and r.m.s. for 1x3 and 3x3 clusters with respect to the $iter_{max}$ method for phase selection. The first two rows demonstrate the effect of shifting the phase of all cells by ± 4 ns. The third row demonstrates the bias when using the method employed by the LArMuID and 3x3 clusters. The final row gives the bias when the phase is determined using the time measured by the Tile calorimeter.*

pulse has a dominant effect. Above the 25$^{\text{th}}$ sample, the ionization current is insufficiently modeled as a result of electrical field variations in the bent section of the accordion. The dependence of this bias as a function of the energy is displayed in Figure 8b. Above 150 MeV, the bias from pulse shape residuals is, as expected, independent of amplitude, and is -2.8%.

For small signals ($E < 150$ MeV), however, an energy dependence of the bias between 5 and 29 sample energy estimates appears. A small pedestal variation (between the database value and the true value during the run, or a drift within the run itself) could result in a bias as a function of the number of samples as demonstrated by the following formula:

$$\begin{aligned} A_{meas} &= \sum_i a_i\,(adc_i - ped_{meas}) \\ &= \sum_i a_i\,(adc_i - ped_{true}) - \sum_i a_i\,(ped_{meas} - ped_{true}) \\ &= A_{true} - \Delta ped \sum_i a_i. \end{aligned} \tag{4}$$

To investigate this effect, the pedestal of each cell, averaged over 1000 events during the cosmic runs, has been compared to the value stored in the database for the relevant run period.[10] Results for a few typical cells are displayed in Figure 9a. Some display a constant shift, while others show a sizeable drift, up to 0.4-0.5 ADC counts. Figure 9b shows, for all the cells, the difference of the average pedestal and database value. A small shift of 0.02 ADC counts is observed with a r.m.s of 0.13 counts. Considering Formula 4, such a number results in an average bias of ~ 0.1 ADC counts, or 1-2 MeV per cell between 5 and 29 samples.[11] When a muon is reconstructed, a few cells are added. Consequently the systematic error attributed to the signal reconstruction depends on the clustering algorithm.

In summary, as a result of the incomplete knowledge of the pulse shape and pedestal values, the uncertainty on the cluster energy from these effects are on the level of 3%.

[10] In a pedestal run the value is computed with 1000 events and 5 samples, resulting in a statistical accuracy of ~ 0.1 ADC counts. In the cosmic case, 32 samples were used.

[11] For 5 samples $\sum a_i = 1.5$, and $\sum a_i = -1.4$ for 29 samples

$\Delta n_{samples}$	bias (%)	$\Delta n_{samples}$	cumulative bias (%)
$5 \rightarrow 7$	-0.97 $\pm$ 0.07	$5 \rightarrow 7$	-0.97 $\pm$ 0.07
$7 \rightarrow 12$	-1.07 $\pm$ 0.05	$5 \rightarrow 12$	-2.04 $\pm$ 0.08
$12 \rightarrow 15$	0.27 $\pm$ 0.03	$5 \rightarrow 15$	-1.77 $\pm$ 0.09
$15 \rightarrow 20$	0.64 $\pm$ 0.06	$5 \rightarrow 20$	-1.12 $\pm$ 0.11
$20 \rightarrow 29$	-1.68 $\pm$ 0.07	$5 \rightarrow 29$	**-2.81** $\pm$ 0.13

Table 4: *Biases in the energy reconstruction versus the number of samples used for the optimal filtering.*

3.3 EM cluster methods

This section examines different cluster methods to measure the total muon energy deposition in the second sampling cells. First, the performance of an algorithm used to identify muons in normal ATLAS running is considered in the cosmic context. Next, a 3x3 cluster is investigated. The aim of this cluster is to capture all the relevant energy deposited in a pseudo-projective muon sample. Lastly, a 1x3 cluster, inherently less sensitive to noise than the 3x3 cluster, is studied in conjunction with an alternative and tighter projectivity selection which limits energy leakage into neighboring cells in η.

3.3.1 LArMuID

A general algorithm to form muon clusters in the EM calorimeter has been developed and is available in Athena as LArMuID [2]. The primary purpose of the algorithm is to tag muons, and it is not optimized to yield the best estimate of the total energy loss of the muon. LArMuID constructs clusters in the following way. The seed of the cluster is the local most energetic cell in the second sampling above an upper threshold. The energies of the neighboring second sampling cells are added when they are above a lower threshold. To be both pure and efficient, the high (low) threshold is set to 5σ (3σ) above the noise. For the noise level in the second sampling using 29 sample optimal filtering coefficients (Figure 7), values of 100 MeV and 50 MeV are chosen for the high and low thresholds respectively. The LArMuID option to include first sampling cells has been disabled in all analyses presented in this note.

Projective muons deposit only a few hundred MeV in a small number of contiguous second sampling cells, as observed in the analysis of test beam data where the cluster size for projective muons was fixed to 2 cells contiguous in ϕ [2]. However, the situation is different in the ATLAS cavern where the cosmic muon trajectories in triggered events are generally non-projective. Figure 10a shows that the number of cells in the LArMuID cluster changes according to the degree of projectivity of the sample (computed with the Tile information, see section 3.1). Because of the threshold to add a cell to the cluster, cells with relevant energy less than 50 MeV will not be included. Hence the true energy will be underestimated by LArMuId, particularly in the case of non-projective muons.

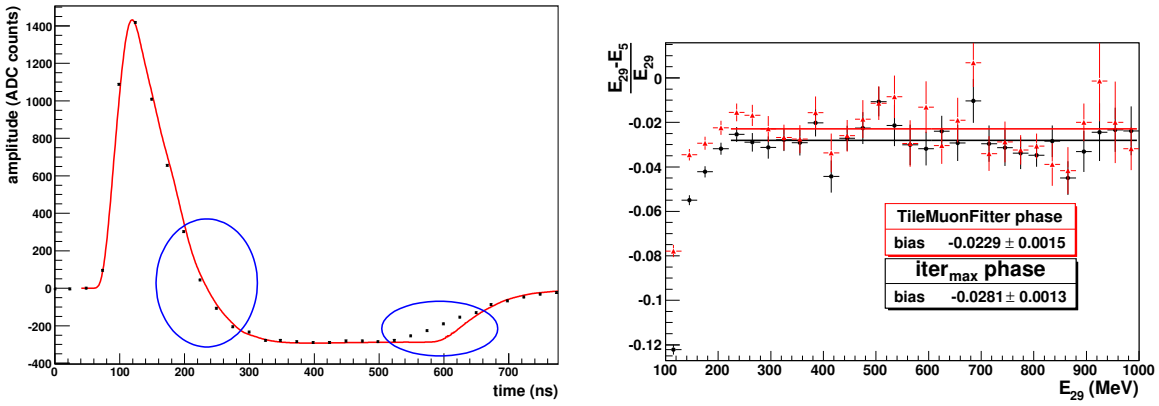

(a) (b)

Figure 8: *(a) A large pulse from an October run is compared to its prediction. The problematic parts of the pulse are illustrated and commented on in the text. (b) Relative energy difference between reconstruction with 29 and 5 samples as a function of the energy reconstructed with 29 samples. Only the maximum energy cell of a muon cluster is used, with a phase determined from the iteration or time from TileMuonFitter (TMF) method.*

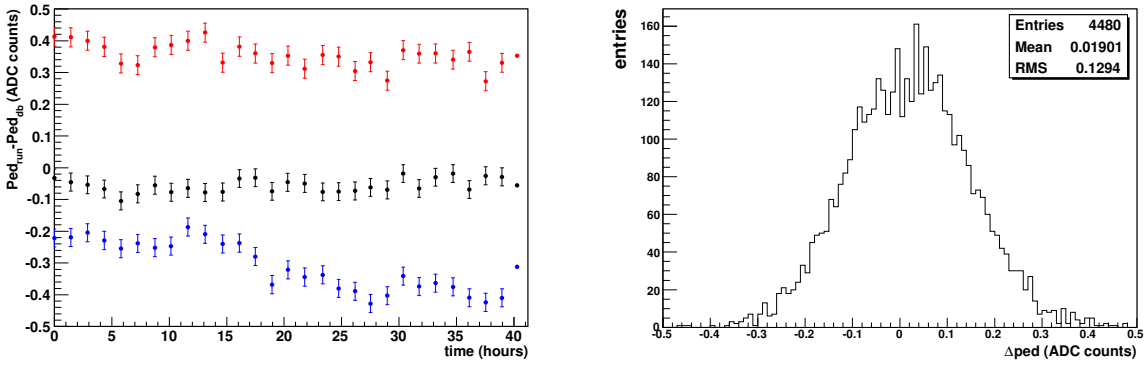

(a) (b)

Figure 9: *(a) Pedestal stability of 3 typical cells averaged over 1000 events as a function of the time of the run. The last point corresponds to the average over the entire run. (b) Difference between the average over the entire run and the value stored in the database for all second sampling cells.*

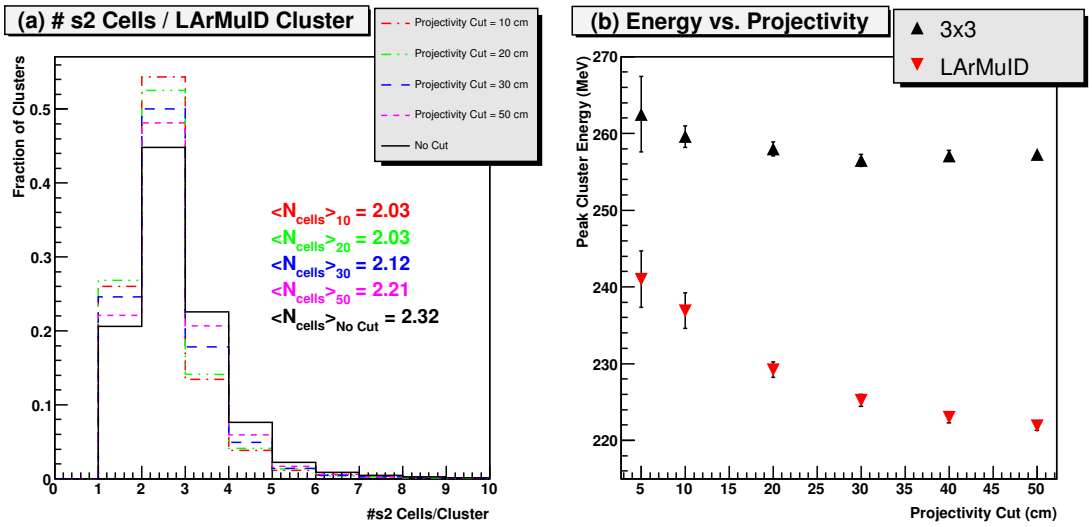

Figure 10: *Impact of the projectivity cut (section 3.1) on: a) the average number of second sampling cells per LArMuID cluster, b) the reconstructed energy for two types of clusters, LArMuID and* 3×3.

3.3.2 Cluster 3x3

A larger size cluster (3×3 cluster centered on any cell 5σ above the noise) has been investigated to recover the energy missed by LArMuID. This cluster method benefits from the very low noise level obtained using 29 samples (section 3.2.1). Figure 10b demonstrates that the reconstructed energy using the 3×3 cluster is less dependent on the projectivity of the sample. Contrary to LArMuId, very little energy is missed outside the 3×3 cluster (the difference in energy between the 3×3 and LArMuID clusters is attributed to this missed energy).

An additional consideration is that on average 40% of the cluster energy is collected in the eight cell ring about the seed cell. As these cells are likely below the threshold to iterate, a fixed phase (discussed in section 3.2.2) is chosen inducing an energy underestimation. As a result the total cluster energy is underestimated by at most 1% (see Table 3).

As the number of highly projective muons in the current sample is small, and some degree of non-projectivity may be tolerated, the 3×3 cluster is a suitable choice for the non-uniformity study (section 5.1). The LArMuId clustering is also used throughout this note as a cross-reference, as it is more adapted for LHC data-taking where the cell occupancy is an issue and only 5 samples will be used in the LAr reconstruction.

3.3.3 Cluster 1x3

The 3x3 cluster is a convenient cluster method which is stable at the level of 1-2% with respect to the projectivity selection. With the limited size of well understood cosmic data presently under consideration, the method does not suffer considerably from the increased noise. However, a 1x3 cluster has also been studied, as it is inherently less sensitive to noise.

In order to use the 1x3 cluster, a novel projectivity selection has been implemented for this cluster to minimize the energy leakage into neighboring cells in η. The selection involves several steps. First, the top and bottom hemispheres are considered separately. An energy deposition greater than 100 MeV is required in a cell in the top or bottom of the second sampling of the EM calorimeter. This cell will be considered the seed of the cluster.

Next, a search algorithm is applied to find the first sampling cell (strip cell) in front of the seed cell which was also traversed by the muon. For a very large fraction of the events, the signal is shared between two strip cells, resulting in a small signal in each. As the signal to noise ratio with 29 samples is about 5 for projective muons in strip cells, identifying the correct one is a difficult task. A search is performed for the maximum energy strip cell in a window of size $\Delta\eta = 0.05$ centered on the second sampling cell, corresponding to 16 strip cells. If the maximum energy strip satisfies both an amplitude larger than 20 MeV ($\sim 3\sigma$ of the noise) and is within $\Delta\eta = 0.025$ of the seed cell, this strip is identified as the correct strip. Out of the $\sim 26\,000$ signals detected in the second sampling, this algorithm has a 40% efficiency.

Lastly, using the seed second sampling cell and the chosen strip cell, projectivity limits are defined according to Figure 11a. These limits are extrapolated to the opposite hemisphere, and the event is accepted or rejected according to whether a significant signal is observed within these bounds in either the second sampling of the EM calorimeter or the Tile calorimeter.

The projectivity selection described above ensures good projectivity in η but not necessarily in ϕ.[12] In Figure 11b, the reconstructed energy for the 1x3 cluster is compared with the total energy deposited and displayed as a function of $\Delta\phi$ ($\Delta\phi = \phi_{up} - \phi_{down} - \pi$, where ϕ_{up} is the position of the top most energetic cell in simulation, and similarly for ϕ_{down}). The 1x2 cluster is also shown for comparison. A selection $\Delta\phi < 0.4$ is chosen in the following. Figure 11c shows the energy containment of the 1x3 cluster relative to the total energy deposited as a function of the 1x3 energy. As demonstrated by the 1x3 energy distribution, most clusters have an energy where $\sim 98\%$ of the energy is measured.

3.4 Correlating EM and Tile measurements

From the full sample of 120 000 events (Table 2) a sample of about 26 000 LArMuID clusters has been extracted. Their spatial distribution is shown in Figure 12. The size of the sample relative to the number of triggered events is a consequence of the rate of noise triggered events ($\sim 50\%$), the incomplete coverage of the trigger towers, the high threshold to initiate a cluster, and the removal of problematic regions (section 2.4). The module M12 contains the greatest number of clusters because it was the only module present in all runs, is located at $\sim -\pi/2$, and was always in the acceptance of the available Tile trigger towers. Additionally, 8 cells in P4 initiated many false clusters as result of incorrect calibration constants due to a faulty calibration line (see Figure 12). However, these cells were already excluded in the detailed analyses as this region was affected by the HV cabling error.

3.4.1 Correlating EM and Tile trajectories

Clusters may not all be initiated by muons but perhaps by noise. In order to assess the purity of the sample of LArMuID clusters, TileMuonFitter is used. Using the trajectory provided

[12] The following results in this paragraph were obtained with simulation.

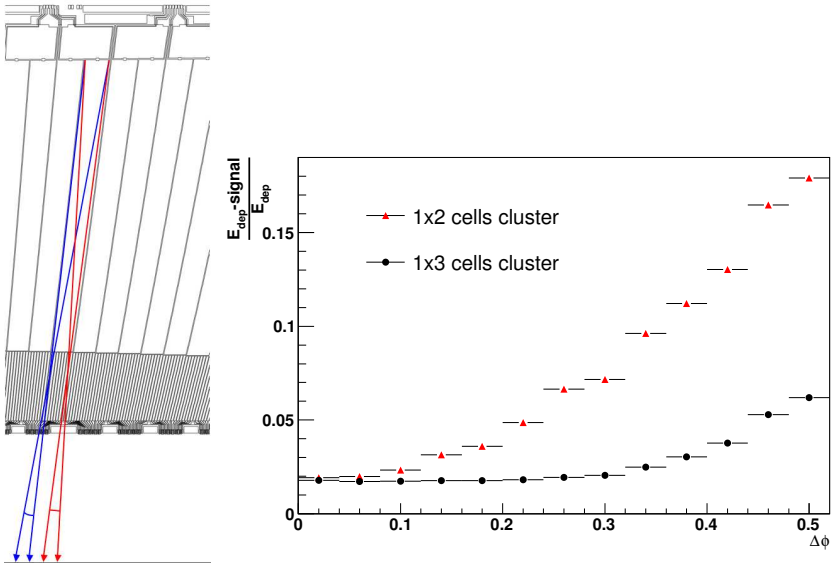

(a) (b)

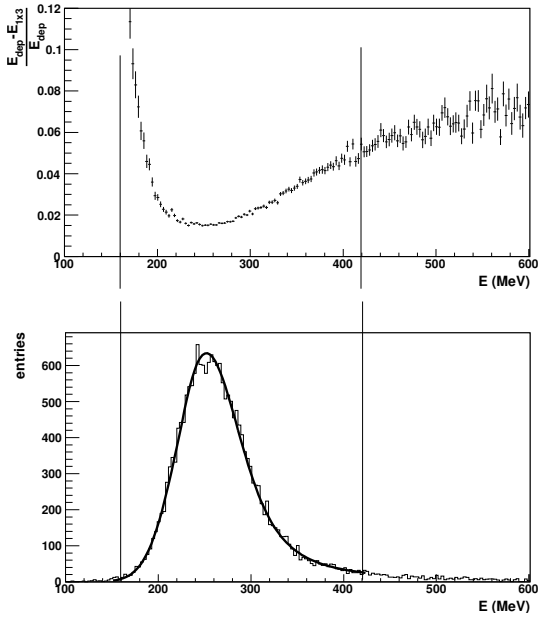

(c)

Figure 11: *(a) Projectivity limits used in the 1x3 cluster method and explained in the text. (b) The energy deposited outside the clusters (1x2 and 1x3 relative to the total energy deposited) is shown as a function of the projectivity ($\Delta\phi$ is defined in the text). (c) The 1x3 cluster provides good energy containment for energies in the bulk of the Landau distribution (simulation with 16 MeV noise per cell matching the noise obtained in a middle cell with 29 samples OFCs).*

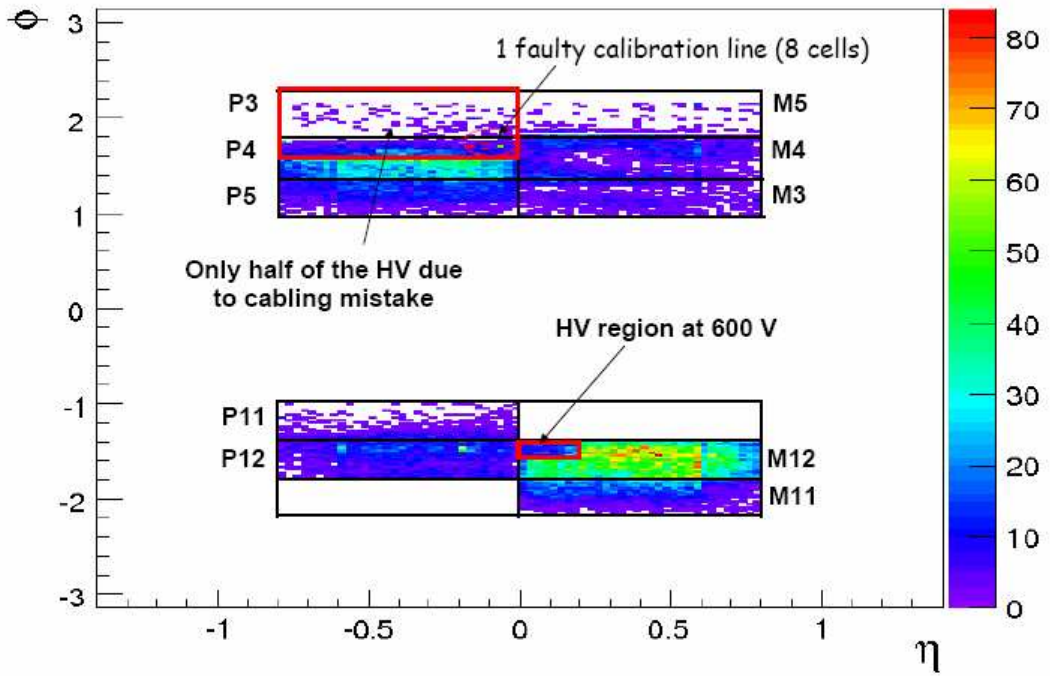

Figure 12: *Number of LArMuID clusters per second sampling cell of the EM barrel Calorimeter for all runs considered in Table 2.*

by TileMuonFitter, one can extrapolate the track to top and bottom EM modules and predict which cells of the second sampling were crossed by the muon. The predicted coordinate of these cells is labeled $(\eta_{tile}, \phi_{tile})$. To validate the reconstruction, LArMuID clusters coordinates (η_{LAr}, ϕ_{LAr}) are compared to the predicted ones. The agreement is assessed with the variables $\Delta\eta = \eta_{tile} - \eta_{LAr}$ and $\Delta\phi = \phi_{tile} - \phi_{LAr}$. As seen in Figure 13, the $\Delta\eta$ and $\Delta\phi$ distributions are centered around zero, ensuring that both sub-detectors are aligned to a few mm. In the region $|\Delta\eta| \times |\Delta\phi| < 0.1 \times 0.1$, $\Delta\eta$ ($\Delta\phi$) distributions can be fitted by a Gaussian of width $\sigma \sim 0.04$, reflecting mainly the Tile granularity.

From Figure 14, it is possible to measure the purity of the muon sample, defining the signal region as $\pm 3\sigma$ of the $\Delta\eta$ and $\Delta\phi$ resolution ($|\Delta\eta| \times |\Delta\phi| < 0.11 \times 0.11$). N_{clus} is the number of clusters in this region whereas the noise contamination N_{noise} is estimated from the side bands ($|\Delta\eta| \times |\Delta\phi| > 0.2 \times 0.2$). The purity of the muon sample is then defined as followed: $(N_{clus} - N_{noise*})/N_{clus}$ where N_{noise*} is the number of clusters normalized to the surface of the region $|\Delta\eta| \times |\Delta\phi| < 0.11 \times 0.11$. In the signal region, the purity can thus be infered to be around 100%. In the case of no Tile information is used, a purity of 90% is obtained.

The precision of the measurement of the (X_0, Z_0) coordinates, provided by TileMuonFitter, can be assessed by comparing them with analogous quantities determined by using events with a top and bottom LArMuID cluster. As (X_0, Z_0) are often used to define a projective sample (see section 3.1), it is necessary to quantify the agreement. In events with two EM clusters, one in the top and one in the bottom, the cluster positions are used to define a trajectory and the cross-point (X_{0LAr}, Z_{0LAr}) computed. Figure 15 shows the distributions of the difference in

ΔX_0 and ΔZ_0 between the LAr and the Tile information. They are centered around 0 and can be fitted by a Gaussian of a width of 6 cm, consistent with the Tile position resolution.

3.4.2 Correlating EM time and Tile time

In the muon time measurement, the time of the maximum second sampling EM cell in each hemisphere is considered. Events with at least one EM cluster analyzed and no requirement on projectivity is made. The EM cell time definition was given in section 3.2.2. As described in section 3.1, TileMuonFitter provides the Tile time measurement at the $Y = 0$ plane.

Figure 16 demonstrates the linear correlation between EM cell time and Tile time at $Y = 0$, corrected for time of flight. The time of flight correction is made to the Tile time and is the distance from the $Y = 0$ crossing point to the EM cell of interest divided by the speed of light. The correction is positive for EM cells with $Y < 0$ and negative for $Y > 0$. All EM cells used in this figure are from the same feedthrough (FT) and have had their signals processed by the same FEB (a given slot in a FT). Lastly, all cells in Figure 16 satisfy an energy selection of greater than 200 MeV, and are thus above the threshold for iteration. The linear fit shown in the figure was first performed without fixing the slope. In this case, the correlation agreed with a unit slope to within 5% and the typical error on the y-intercept was ~ 2 ns. After fixing the slope to be unity, the error on the y-intercept decreased to just below 1 ns.

As a validation of the time of flight correction method above, events with a top and bottom EM cluster were used to determine the geometric time of flight between the top and bottom EM clusters. The Tile measurement was the same as that described above, but this time the trajectory is extrapolated both above and below to the EM cells of interest. For the events in this sample, the time of flight comparison showed a good linear correlation between Tile and EM from 11 ns to 15 ns with an agreement of ~ 120 ps.

4 EM Calorimeter commissioning with muons

4.1 Scan for dead cells

A complete map of dead cells has been extracted from electrical measurements [3] and concerns less than 0.02% of the cells. Cosmic muons offer the first opportunity to identify dead cells for physics over a large acceptance. The detection of dead channels is easier in the second sampling, compared to the first and third, because of the higher signal to noise ratio. A cell is defined to be dead if it has not initiated a LArMuID cluster while its 8 neighbors have at least 5 times. In this case, the probability to mistake a good cell for a bad one is, for example, 0.42% for the module M12 which was present in all runs and collected of 14758 LArMuID clusters. With this criteria, and the present sample size, dead second sampling cells were searched for over 6% of the barrel acceptance (Figure 12). None were found.

The signal to noise ratio in the first sampling is less favorable for searching for dead cells. Nevertheless, by looking at first layer cells in front of second sampling LArMuID clusters and selecting them via a cut on energy at 30 MeV (4σ), a sample of ~ 7400 hits in the first sampling is extracted. The two plots of Figure 17 present the map of the number of hits per first sampling cell. It allows, in the most populated region (with a mean of 5 hits per cell) which represents about 15% of the scanned region, to detect dead first sampling cells. In this case the probability

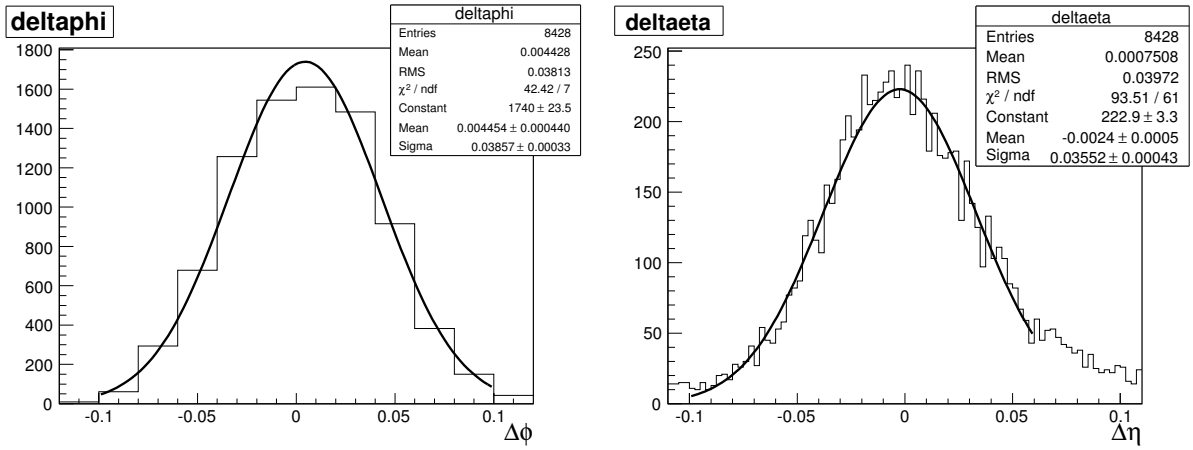

(a) $\Delta\phi = \phi_{Tile} - \phi_{0LAr}$ (b) $\Delta\eta = \eta_{Tile} - \eta_{0LAr}$

Figure 13: *Comparisons of* ϕ *and* η *reconstructed in LAr and in Tile.*

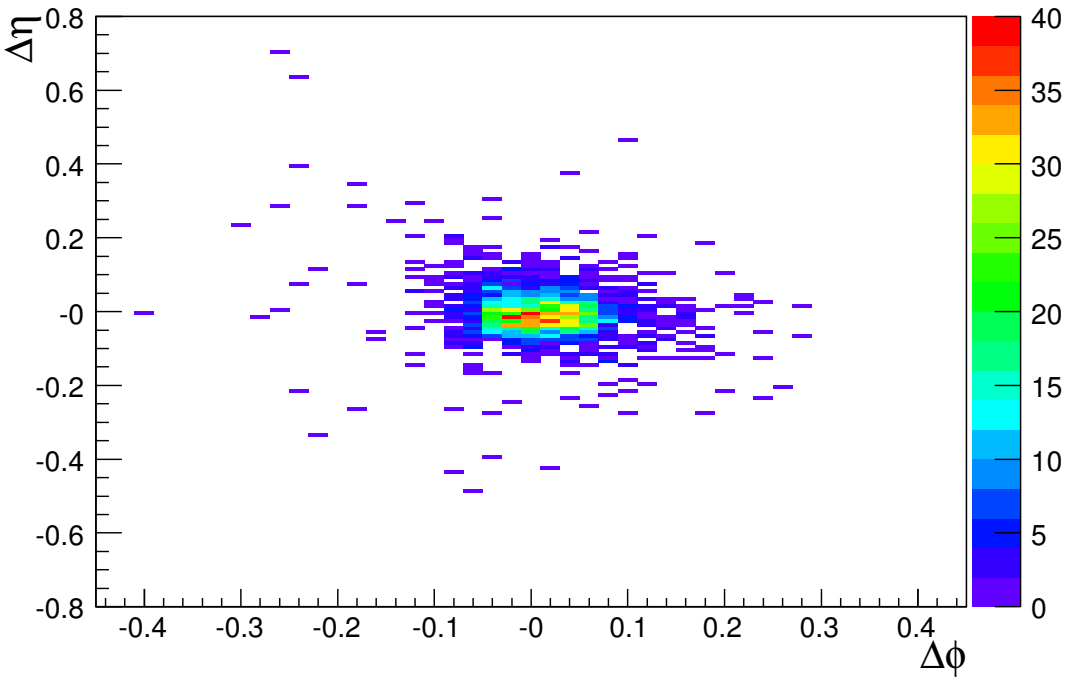

Figure 14: *Comparisons in the* η *and* ϕ *plane of reconstructed clusters in LAr and Tile tracks for August run 7811.*

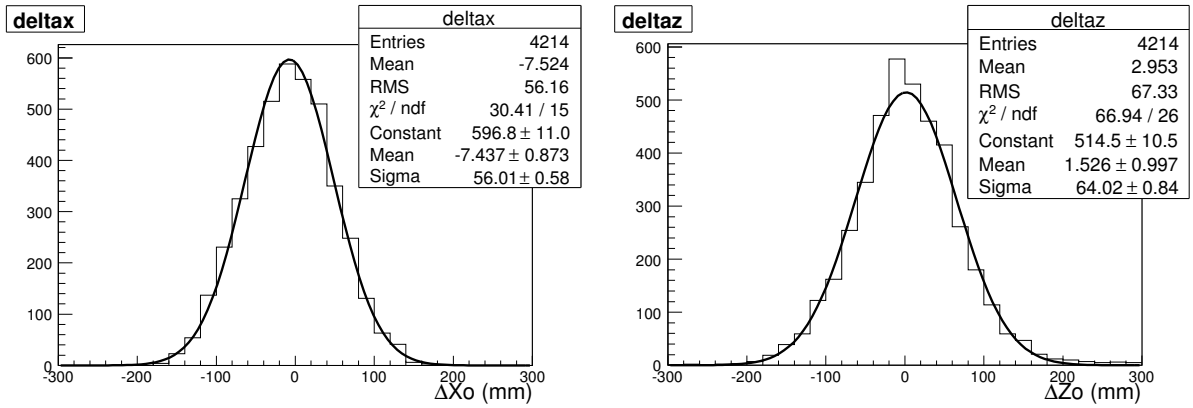

(a) $\Delta X_0(mm) = X_0 - X_{0LAr}$

(b) $\Delta Z_0(mm) = Z_0 - Z_{0LAr}$

Figure 15: *Comparison of* (X_0, Z_0)*, the coordinates of the crosspoint from Tile reconstruction and* (X_{0LAr}, Z_{0LAr})*, coordinates extrapolated from matching EM clusters. Events require 2 matching clusters one at the top and one at the bottom, a straight line is then defined between them and the track is extrapolated at* $Y = 0$*.*

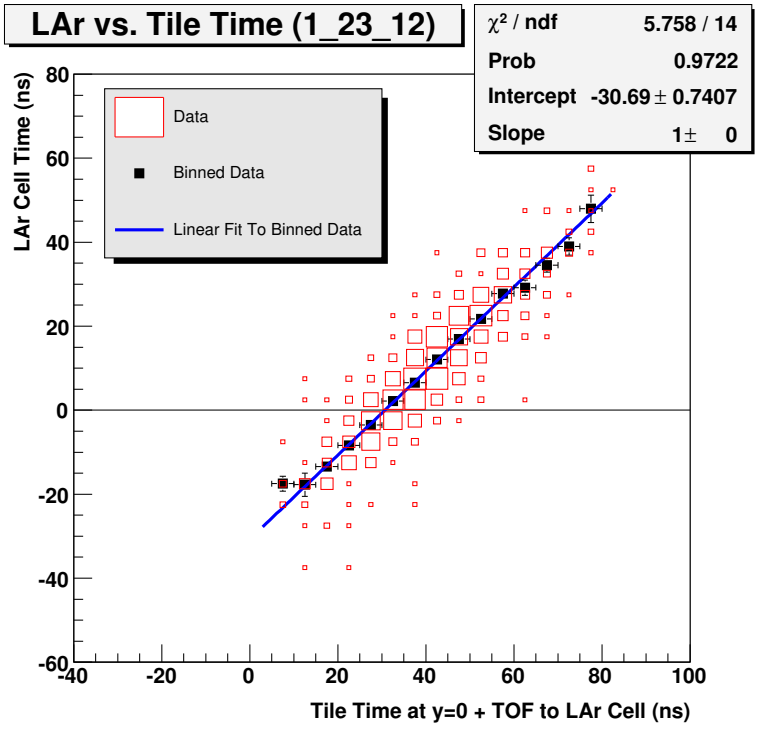

Figure 16: *EM cell time vs.Tile Time at* $y = 0$ *corrected for time of flight. Data is from Side A (1), FT 23 of Module M12, FEB Slot 12.*

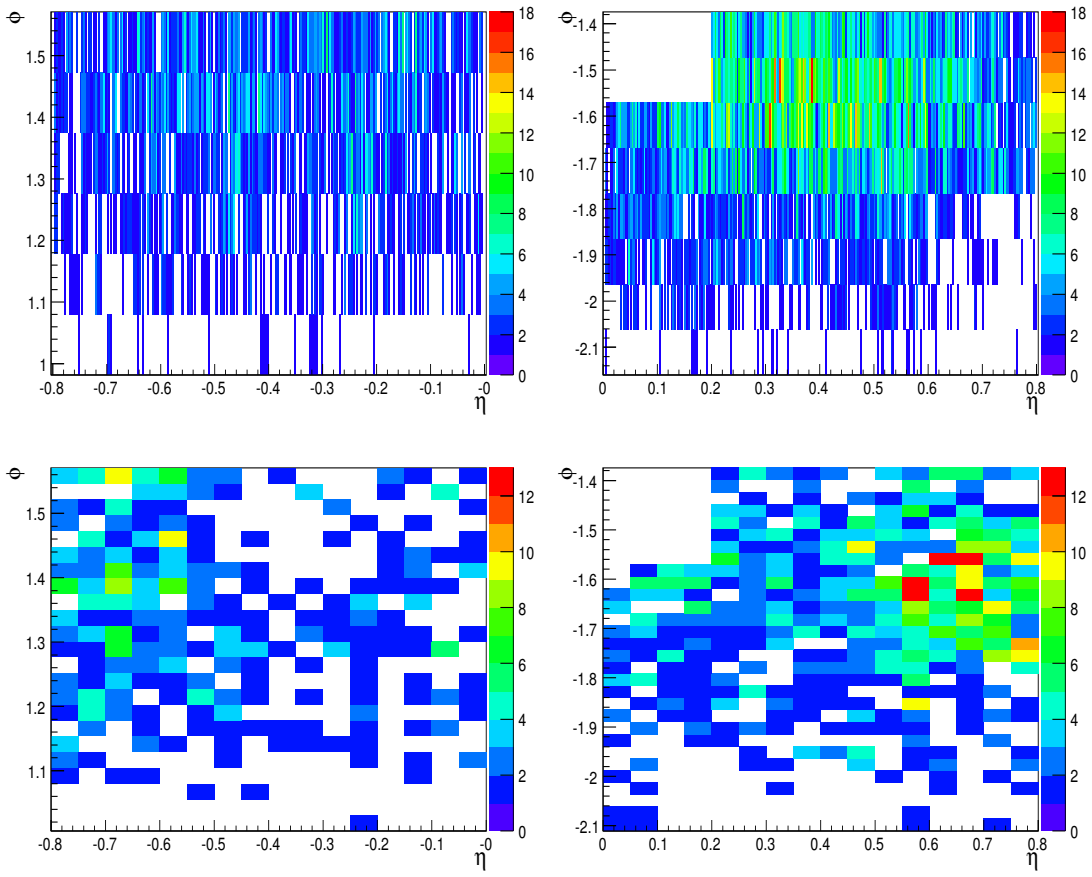

Figure 17: *Number of muon hits per first sampling cell in top P4 and P5 modules (top left) and in bottom M12 and M11 modules (top right). Number of muon hits per third sampling cell in the top P4 and P5 modules (bottom left) and in the bottom M12 and M11 modules (bottom right).*

to mistake a good cell for a bad one is, for example, 0.4% for module M12. None were found. In the less populated region approximately ~ 4 times more data is required in order to make a search.

The signal to noise ratio in the third sampling is even less favorable. To extract signal third layer cells, the same method is used as above. Third layer cells are searched for behind second layer LArMuID clusters and selecting them via a cut on energy at 4σ (53 MeV for $|\eta| \leq 0.5$ and 57 MeV for $|\eta| > 0.5$). The bottom two plots of Figure 17 present the map of the number of hits per S3 cell. The available statistics ($\sim$ 1200 hits) does not allow one to make a conclusion on the presence of dead third sampling cells.

4.2 Region with HV at 600V

One of the HV zones of the scanned regions, pointed out in Figure 12 and affecting M12, is supplied by a voltage of 600V (section 2.4). This zone draws a current above the usual value of a few μA. Such anomalous zones (only several from the total of 896 in the barrel

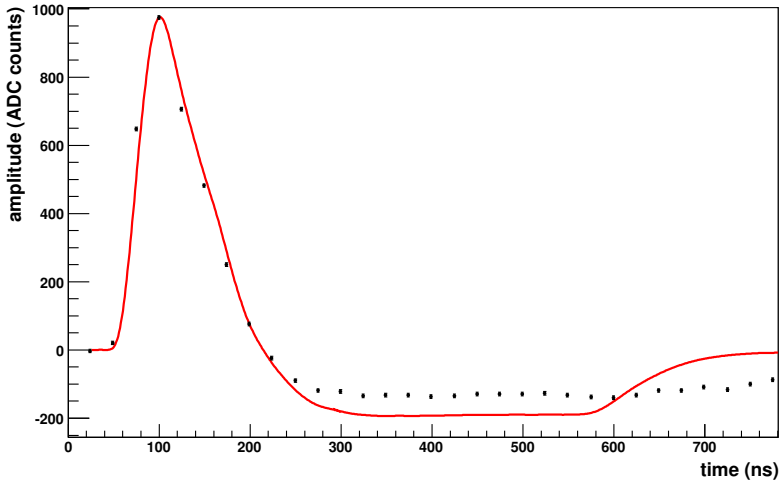

Figure 18: *Example of large amplitude physics pulse in a second sampling cell in a region with HV = 600 V. The pulse is compared with the predicted physics signal assuming a drift time corresponding to HV = 1600 V (solid line). The undershoot can easily be observed, but is less pronounced than at higher HV values.*

calorimeter) have been supplied with a lower voltage in order to fulfill the condition that less than 1W is deposited in the LAr bath. This configuration was tested during the October run period. The signal response at 600V is reduced by 40% compared with the nominal value (Appendix 2). Under these conditions, several high energy depositions (signals in excess of 500 MeV) were observed in the second sampling, as illustrated in Figure 18. This is the first validation with physics signals of the aforementioned configuration which avoids the loss of acceptance. Additionally, it was also demonstrated that no additionnal noise in ADC counts was measured in the corresponding region.

5 EM Calorimeter performance with muons

Despite the statistically limited sample, the barrel EM calorimeter performance is considered in this section. In section 5.1, the muon energy measurement is used to study the variation in η of the response of the second sampling. Initial studies of timing uniformity and resolution are presented in section 5.2.

5.1 Detector non-uniformity in η

The response of EM calorimeter cells to electrons was measured in 10% of the modules with 2001-2002 test beam data and agreed with the expected values to better than 0.5% [11]. Cosmic muons provide a good opportunity to study the calorimeter response to muons *in situ* with more modules before the start of the LHC. Most response non-uniformities arise in the η direction due for instance to the cell inductance variations. In contrast, the ϕ symmetry of detector components ensures very low non-uniformity along this direction. In this section it is shown that

the response variation in η of the second sampling can be probed at the level of 2% in η bins of 0.1 width with the present sample of well understood cosmic muon data. An estimation of the number of projective events necessary to probe individual cell non-uniformities is provided.

5.1.1 Parameter extraction from the distribution of energy depositions

Cosmic muons may be considered minimum ionizing particles (MIPs) and their energy depositions therefore follow a Landau distribution. As shown in Appendix 1, the most probable value (MPV) of the Landau distribution scales linearly with the path length and logarithmically with the incident energy. Therefore, the cell response, quantified by the MPV, is expected to track the η dependence of the cell depth as displayed in Figure 2.

To illustrate how the non-uniformity study is performed in this note, we first consider an idealized situation which will also help to identify the major systematic errors. Suppose that cosmic muons are mono-energetic and that the data sample may be considered infinite. In this case, for any given cell in η, a selection can be made to consider only those muons which passed through the cell with a purely projective trajectory. In the absence of detector noise, the distribution of measured energy depositions in this cell will follow a Landau distribution with an MPV proportional to the cell depth.

The connection of this ideal situation to the real one is made by first removing the assumption of mono-energectic muons. Instead of a single Landau energy distribution, the distribution becomes a superposition of many Landau distributions according to the cosmic muon energy spectrum. As the dependence on energy is only logarithmic, and the cosmic muon energy spectrum falls rapidly, the energy distribution for cosmic muons is expected to remain very close to a Landau.

Next, the reality of a limited sample size is considered. The present sample of well understood cosmic muon data is too small to allow for a study with only projective trajectories and η granularity at the level of a single cell. When considering the LArMuID and 3x3 clusters,we allow a certain degree of non-projectivity, and hence trajectories with a variable number of cells traversed and a variable path length in each cell (section 3.3 discussed the performance of the LArMuID and 3x3 cluster algorithms in pseudo-projective muon samples). Consequently, we will not attempt to make a plot of individual cell MPV vs η, but rather use the cluster energy and the η of the cell in the cluster with the maximum energy. The MPV is obtained from cluster energy histograms which have been separated according to maximum cell η intervals of 0.1 in the range $-0.8 < \eta < 0.8$. We will assume that despite the variation in path lengths the resulting energy distributions remain approximately Landau.

Finally, as discussed in Section 3.2.1, the individual cell noise is a significant fraction of the total signal deposited by the muon. The correct fit hypothesis is therefore a Landau convoluted with a Gaussian distribution whose width, σ_G, should represent the noise contribution from the cells which compose the cluster.

Figure 19 displays the measured energy distribution for LArMuID and 3x3 clusters in the range $0.3 < |\eta| < 0.4$ and any value of ϕ. [13] The clusters are from $\sim 10,000$ events which satisfy

[13] In the following, only October 2006 and March 2007 data are used for this study, as this avoids a systematic error associated with combining data sets taken with different HV settings.

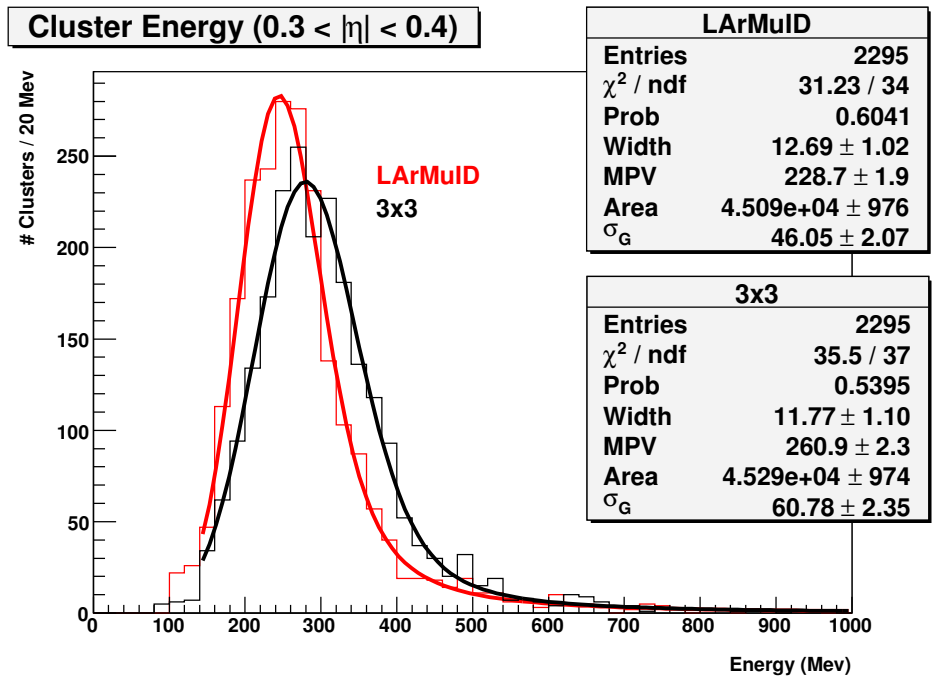

Figure 19: *Measured LArMuID and 3x3 cluster energy distributions in the range* $0.3 < |\eta| < 0.4$*, using the* $(|X_0|, |Z_0|) < (30\,\text{cm}, 30\,\text{cm})$ *pseudo-projectivity selection criteria for data.*

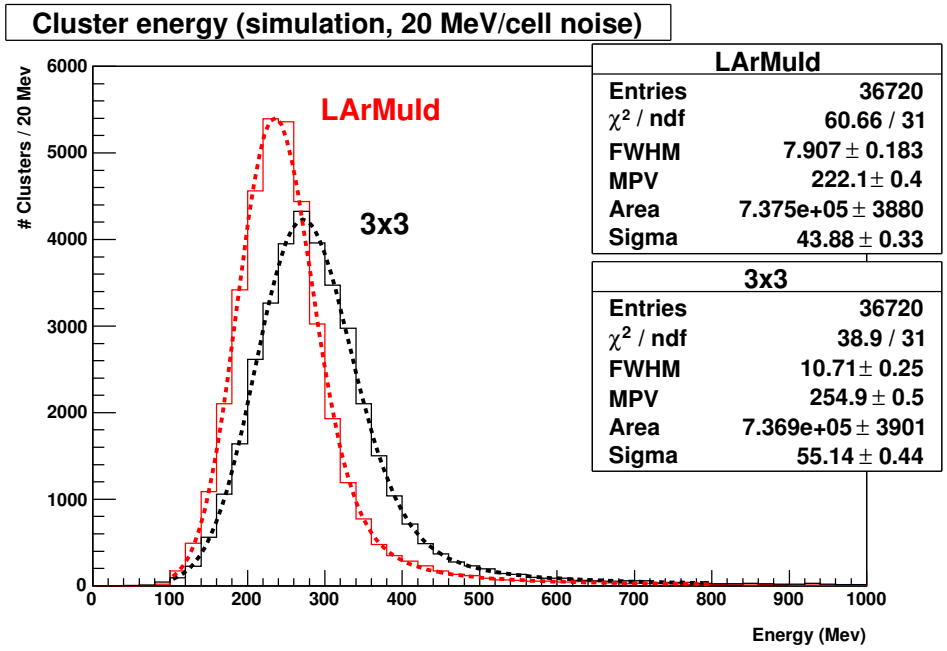

Figure 20: *Simulated LArMuID and 3x3 cluster energy distributions in the range* $0.3 < |\eta| < 0.4$*, using the* $(|X_0|, |Z_0|) < (30\,\text{cm}, 30\,\text{cm})$ *pseudo-projectivity selection criteria.*

the pseudo-projectivity selection $(|X_0|, |Z_0|) < (30\,\text{cm}, 30\,\text{cm})$ (section 3.1). The χ^2/NDF of both fits strongly supports the choice of a Landau convoluted with a Gaussian as the fit function which describes the data. Figure 20 shows similar plots obtained in the monte carlo (MC) simulation. The same distribution was shown for the 1x3 clusters in Figure 11. The ϕ uniformity of the response was first checked by looking at the cluster energy distributions separated in ϕ regions ~ 0.2 radians wide, corresponding to one feedthrough (FT). Using the six FTs which account for 86% of the total number of clusters, the MPV for each FT energy distribution agreed with the average MPV to within 2% for both cluster methods. The error on each MPV value was $\sim 1\%$ for all cluster methods. Further, the fitted σ_G and Landau width (w) values for each FT and cluster method were consistent within their errors.

Having established the quality of the fit in 0.1 η bins, and justified the assumption of azimuthal symmetry, the properties of the energy distribution as a function of η may now be examined in more detail. In contrast to ϕ, all fitted parameters $\{\text{MPV}, \sigma_G, w\}$ are expected to vary in η. This dependence is discussed in the following sections.

5.1.2 η dependence of the Gaussian width and Landau width

Figure 21a shows the value of the Gaussian width parameter, σ_G, as determined from fits of the energy distribution binned according to $|\eta|$ intervals 0.1 units wide. The single cell noise is also shown, scaled by 3 for comparison with the 3x3 cluster σ_G and $\sqrt{2.12}$ for comparison with LArMuID (2.12 is the average number of cells per cluster for this pseudo-projectivity selection, see Figure 10a). The $\sim 5\%$ increase in the noise data with η is a result of the increased detector capacitance due to the increased cell size. The fitted values of σ_G for the 3x3 cluster are consistent with the interpretation that the value is determined by the uncorrelated noise contribution of 9 cells. With the present sample size the precision is not sufficient to track the slight η dependence.

The fitted values of σ_G for the LArMuID cluster, on the other hand, do not support the interpretation in terms of individual cell noise. An explanation of this discrepancy is that the noise contribution of ~ 2 cells is small in comparison with other systematic effects, such as missed energy from the high threshold to add a cell to the cluster and variable path length.

Figure 21b shows the fitted value of the Landau width w and the values found in the MC analysis using true clusters. As explained in Appendix 1, w also scales linearly with the path length. The fitted values for both the 3x3 and LArMuID clusters are consistent with the expected values but the precision is presently insufficient to track the η dependence. Similar conclusions for w and σ_G apply for the 1x3 cluster as well.

5.1.3 η dependence of the most probable energy

Previous sections established that the distribution of muon energy depositions in η intervals of 0.1 fit well to the Landau convoluted with Gaussian hypothesis, and that the fit parameters are well understood. The fact that the Gaussian noise contribution and the Landau width fit well for the 3x3 cluster to noise data and Monte Carlo respectively strongly suggests that the aforementioned systematic errors (cosmic energy spectrum and variable path length) are currently comparable or below the present statistical errors. Therefore, we are now in a position to consider the η dependence of the MPV.

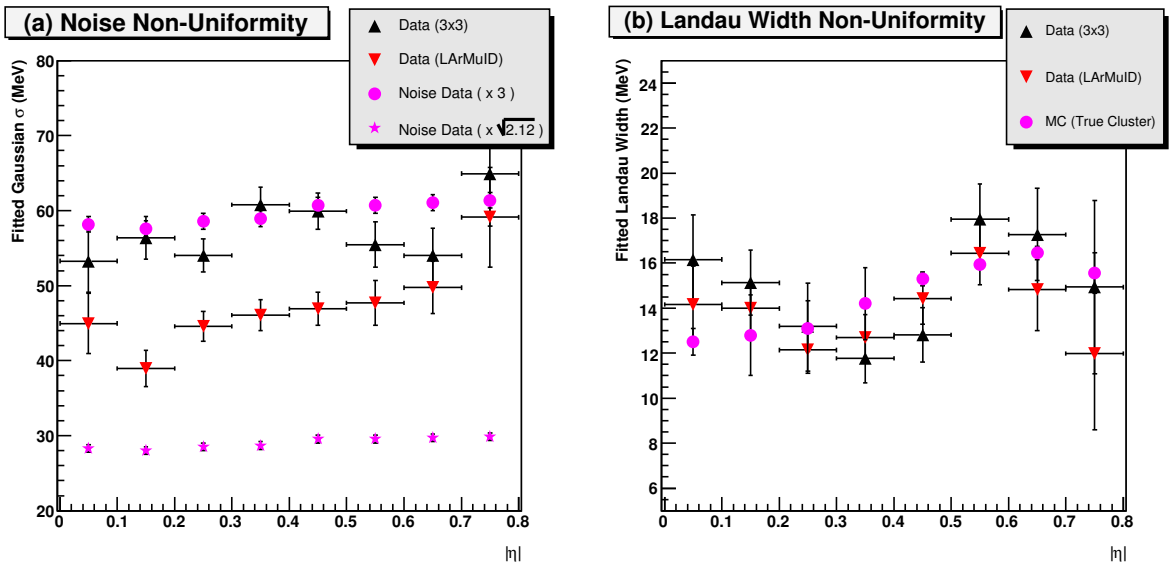

Figure 21: *(a) Fitted Gaussian* σ *vs* $|\eta|$. *(b) Fitted Landau width vs* $|\eta|$.

Figure 22 presents the MPV values of all cluster methods as determined from the fits of the energy distributions binned in η intervals with a width of 0.1 from $-0.8 < \eta < 0.8$. The dependence of the MPV on η is compared to the true cluster values found in the MC analysis corresponding to the same event selection. GEANT 4.7 (standard physics list) was used for the simulation. It is now understood that GEANT 4.8 better describes the actual sampling fraction for electrons as a result of a more realistic treatment of multiple scattering. As the μA to MeV calibration constant, which is needed to calculate the deposited energies in the cells, has decreased between the two versions, the MC results have been scaled accordingly by -12.5%.[14]. Several energy scale corrections have been applied to the data. First, the data have been scaled up by 8.8% in order to reference the response to that expected at the nominal HV value of 2kV (see Appendix 2). Further, LArMuID and 3x3 cluster data have been scaled up by an additional 1% to account for using a fixed phase in reconstructing cells in the cluster which are below the iteration threshold (section 3.2.2). Lastly, LArMuID and 1x3 data have been scaled up by a final 3% to account for energy lost as a result of cross-talk with neighbor η cells (measured with muon data). The remaining difference in energy between the LArMuID and 3x3 clusters is attributed to missed energy (section 3.3). The 3x3 and 1x3 cluster energy agree statistically with the MC true cluster in the overall energy scale to about 3%. However, there are systematic uncertainties which amount to a total uncertainty of at least 5% (2.5% from MC normalization, 3% for the bias between 5 and 29 sample signal reconstruction, and some uncertainty on the absolute electronic calibration that is still under study).

Figure 23 presents the normalized MPV values of the data and MC presented in Figure 22a. The expected second sampling cell depth numbers are shown superimposed (also normalized). The η dependence of the data is in good agreement with the MC simulation and expected cell depth at the level of $\sim 2\%$. A sample size larger than the one used here ($\sim 10,000$

[14]This number currently has a 2.5% systematic uncertainty.

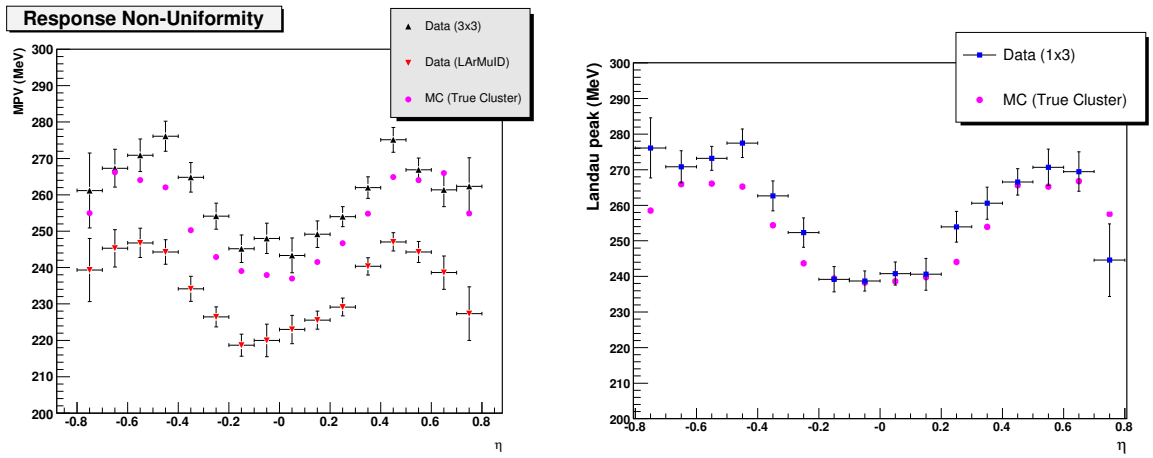

(a) (b)

Figure 22: *(a) Most probable energy value vs* η *for LArMuID, 3x3 clusters, and MC true clusters. Projectivity selection is* $(|X_0|, |Z_0|) < (30\,\text{cm}, 30\,\text{cm})$ *(section 3.1). (b) Most probable energy value vs* η *for 1x3 clusters. Projectivity selection is defined in section 3.3.3.*

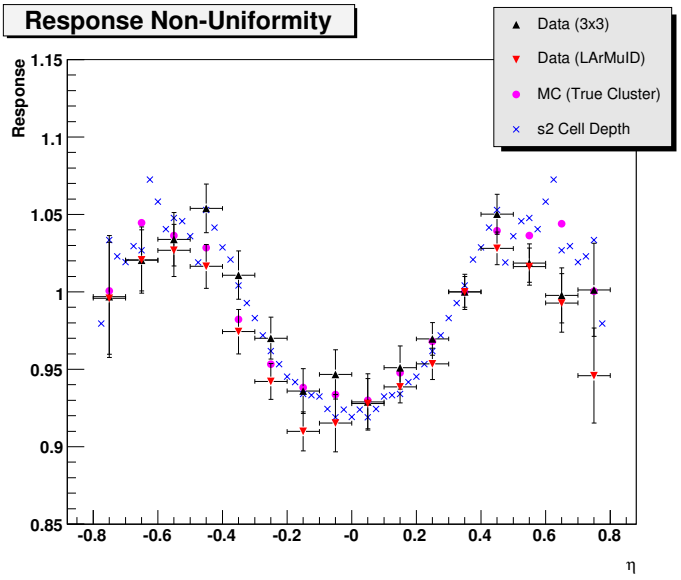

Figure 23: *Data and Monte Carlo shown in Figure 22a, and expected second sampling (s2) cell depth, normalized to the* $0.3 < \eta < 0.4$ *bin.*

events) would allow for a similar analysis but with a finer binning in η. To probe the true detector non-uniformity for individual cells at the level of $\sim 1\%$ would require approximately $\sim 160,000$ pseudo-projective events. This extrapolation is purely statistical and no systematic effects are included. Clearly, as the η binning is decreased, and the desired precision increased, the projectivity requirement must be tightened. Hence, an additional factor to account for a more projective sample is necessary. Additionally, to understand the cell depth at the level of $\sim 1\%$ requires a better understanding of the effect of the cosmic muon energy spectrum and how the spectrum is modified by the presence of the shafts (see Appendix 1).

5.2 Muon time measurement

The timing resolution of the EM calorimeter was studied with 2001-2002 test beam data [2, 12]. This section presents initial studies of the EM time measurement using cosmic muons. The linear relationship between the EM cell time and the time determined by the Tile calorimeter has already been discussed in section 3.4.2. Figure 16 demonstrated the correlation for one front end board (FEB), and the y-intercept represents the timing offset of this FEB with respect to Tile. The collection of timing offsets allows for a first look at timing uniformity. This topic is discussed in section 5.2.1. Section 5.2.2 examines the spread of the data about the fitted linear relationship with the aim of assessing the timing resolution.

5.2.1 Timing uniformity

Figure 24 displays the timing offsets for FEBs in the October 2006 data.[15] The value of the offset represents a time shift relative to the Tile calorimeter. For the same trigger, larger offset values reflect a later signal arrival time relative to the time of flight corrected Tile time. Figure 24 reveals two interesting features. First, there appears to be a shift between side C and side A which suggests that side C signals are arriving later. Second, a shift between slot 11 and slot 12 is observed, suggesting that slot 11 signals are arriving later.

A hypothesis to explain the shift between side A and side C has been formulated based on the trigger configuration during this run period. The data were taken without the central trigger processor (CTP). Instead, two chained local trigger processors (LTPs) were used, where the LTP for side A was the master and the LTP for side C was the slave. The signal arrived to LTP-C along a ~ 5 ns cable from LTP-A. The hypothesis is that the shift is a result of this additional cable length. The trigger for side-C would have requested samples which were later than those for side A. If these samples were indeed later it would appear that the waveform arrived earlier for side C than side A. This conclusion is supported by Figure 24.

Concerning the shift between slot 11 and slot 12, the calorimeter has been cabled such that signals induced in cells from particles originating at the interaction point (IP) should arrive at the FEBs at the end of the barrel at approximately the same time. Lower η cells are closer to the interaction point (IP). To compensate, higher η cell are given correspondingly shorter cables to account for this path length difference (IP to cell). The timing offsets shown in Figure 24 are sensitive to the cell to FEB travel time only, as the cosmic muon time of flight has already been accounted for. Therefore, slot 11 signals should appear to arrive later by the difference of

[15] Only second sampling cells are considered. Slot 11 serves second sampling cells from $0 < |\eta| < 0.4$, while slot 12 serves second sampling cells from $0.4 < |\eta| < 0.8$.

the typical IP to cell at $0.4 < |\eta| < 0.8$ time and the typical IP to cell at $0.0 < |\eta| < 0.4$ time. Figure 24 is consistent with Slot 11 signal arriving later. A time of flight difference of ~ 2 ns is expected and approximately seen in Figure 24.

Lastly, timing variations are expected within a FEB. An approximately ~ 2 ns "V" shaped variation of time offsets as a function of channel number exists due to the signal propagation within the board. This shape has not been accounted for, as it is a small effect ($\sim 2\,\text{ns}/\sqrt{12}$) with respect to other contributions, such as Tile timing uniformity and resolution (see section 5.2.2), found in this analysis. Hence the time offset can be viewed as averaging over the "V" dependence.

5.2.2 Timing resolution

The scatter of the data about the fitted line in Figure 16 is determined by the combined resolution of the EM and Tile time measurements. Taking the correlation slope to be one (section 3.4.2), the width of the distribution of EM time minus the time of flight corrected Tile time yields the combined resolution. The offset discussed in 5.2.1 is included to center the distribution for each FEB at 0. Once centered, the time difference distributions of different FEBs are combined to increase the size of the sample. Lastly, the sample is broken into different bins of EM cell energies. One expects that the time resolution decreases with the inverse of the energy.

Figure 25 presents the results of this analysis using October 2006 data. The results given here are consistent with the preliminary analysis originally reported in [14]. The vertical axis gives the resolution, which is defined as the width of the distribution as determined by a Gaussian fit. The figure shows the dependence of the resolution on the energy of the LAr cell. The resolution data are fit to the quadrature sum of a constant (*Res* with time-energy units) divided by energy and another constant (*Const*, with time units). The value of *Res* is comparable with the value 1420 MeV ns determined in test beam [2, 12]. However, the value of *Const* is larger than the 0.65 ns test beam value. Independent studies of Tile timing uniformity and resolution indicate that these are contributing effects. The timing resolution of an individual Tile cell was found to be 1.6 ns, and the uniformity was at the level of 2 ns with a small number cells out of time by 5-10 ns.

A different method for evaluating the EM cell time resolution has been investigated which does not rely on a comparison with the time determined from Tile. In this method, events with a top and bottom EM cluster are used. The time of the maximum cells in the cluster are compared, if both these cells are above the 150 MeV threshold to iterate. Time of flight and timing offset corrections are made. As the number of events with large energy depositions in both the top and bottom of the calorimeter are a small fraction of the total, this method is statistically limited compared to the one described above. The *Res* value determined from this method is 1288 ± 171 MeV ns, and the *Const* value was found to be 2.6 ± 1.6 ns.

6 Conclusions and outlook

The cosmic data taken with the barrel EM and Tile calorimeters between October 2006 and March 2007 have been analyzed and the results are presented in this note. The analysis tested the full signal recontruction chain for EM signals, which includes pedestal subtraction, pulse

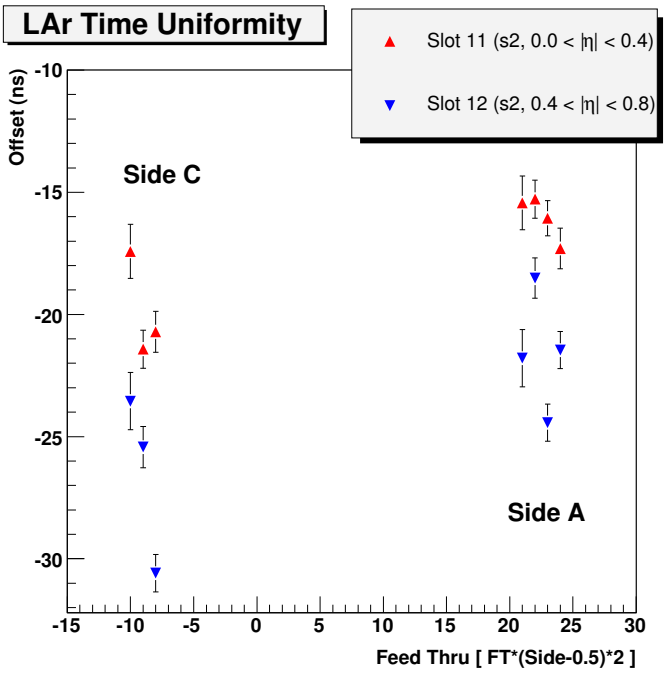

Figure 24: *EM time offsets relative to Tile for different LAr FEBs. For A (C) side, side=1 (0) in the x-axis.*

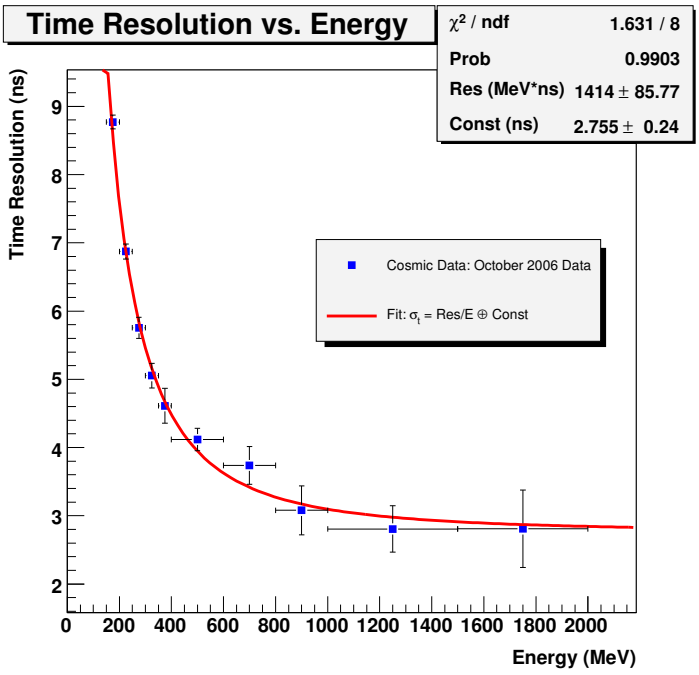

Figure 25: *Dependence of Time Resolution on LAr cell energy.*

shape prediction, amplitude and time determination using the optimal filtering technique, and energy scale calibration. The overall energy scale has been shown to agree with simulation to within 3% for typical cosmic energy depositions. Additionally, unique signal reconstruction techniques have been employed in order to overcome certain challenges presented by the cosmic situation. These techniques include noise reduction by using additional samples and iteration for OFC phase selection.

The muon sample extracted from 120 000 triggered events consists of approximately 30 000 electromagnetic clusters distributed in 9 barrel modules. Using Tile calorimeter information, the sample has been shown to be very pure and the location of these clusters correlate well with the extrapolation of the trajectory determined by Tile. The clusters have been used to perform several commissioning tasks. For example, HV cabling errors were discovered with this sample, and a search for dead cells in regions with sufficient data has been performed. Also, physics signals in regions with non-nominal HV have been observed. Lastly, although statistically limited, the sample has been used to used to study detector response unifomity and timing performance. The non-uniformity of the second sampling was shown to be less than 2% in 0.1 η bins in the region $-0.8 < \eta < 0.8$. The timing uniformity among the front end boards of the instrumtented modules was probed at the level of 1 ns and a timing resolution of $\sim 3 \pm 2$ ns was observed.

Since March 2007, cosmic data have been collected nearly every weekend. In addition, three ATLAS miltestone weeks have taken place, resulting in further cosmic data. The number of instrumented modules in both the EM and Tile calorimeter has steadily increased since the period under consideration here. Thus, this note constitutes a demonstration of the potential of the cosmic analysis. Commissioning studies, such as those described in secion 4, may now be carried out on nearly the entire LAr calorimeter (this includes the electromagnetic and hadronic end-cap). Also, performance studies, such as those described in section 5, will benefit greatly from an increased sample size. As the first LHC collisions are at least several months away, the analysis of this data is an important commissioning task and an invaluable means to prepare for first collision data.

7 Acknowledgments

We are privileged to have had the opportunity to analyze the first cosmic data of the ATLAS LAr calorimeter collected inside the cavern at Point 1. The analysis of the first cosmic muon events would not have been possible without the dedicated effort of many people in our LAr detector group and the ATLAS collaboration over many years. We are especially indebted to those who built, integrated and installed the LAr detector in the ATLAS cavern, and those who operate the detector on a daily basis. We are very grateful to our colleagues who have built and now operate the high voltage system, the low voltage system, the cooling system, the cryogenics system, the read-out system and software, and those who wrote the reconstruction software. We are indebted to our technicians for their contribution to the construction and running of our detector. We would also like to warmly thank our colleagues from the Tile Calorimeter group, who supplied us with a trigger for the cosmic muon runs and kindly stopped other commissioning activities to join us during the frequent combined cosmic data taking.

References

[1] A. Camard et al., *Study of the EM Barrel Module 0 with muons*, ATL-LARG-2001-017.

[2] M. Aharrouche et al., *Caracterization of the ATLAS electromagnetic liquid argon calorimeters with muons*, NIM paper in preparation.

[3] ATLAS Electromagnetic Liquid Argon Calorimeter Group, *Construction, assembly and tests of the ATLAS electromagnetic barrel calorimeter*, Nucl. Inst. Meth. A **558** (2006) 388.

[4] The ATLAS Collaboration, *The ATLAS Experiment at the CERN Large Hadron Collider*, ATL-COM-PHYS-2007-087.

[5] K. Anderson, J. Pilcher, H. Sanders, F. Tang, and R. Teuscher, *Stand-alone Cosmic Ray Trigger Electronics for the ATLAS Tile Calorimeter*, Proceedings, 10th Workshop on Electronics for LHC and Future Experiments, September 13-17, 2004, Boston, USA.

[6] https://twiki.cern.ch/twiki/bin/view/Atlas/TileMuonFitter.

[7] W.E. Cleland, E.G. Stern, *Signal processing considerations for liquid ionization calorimeters in a high rate environment*, Nucl. Instrum. Methods A338, (1994), 467-497.

[8] ATLAS Electromagnetic Barrel Calorimeter Collaboration, *Energy linearity and resolution of the ATLAS electromagnetic barrel calorimeter in an electron test-beam*, Nucl. Inst. Meth. A **568** (2006) 601.

[9] D. Banfi, M. Delmastro, M. Fanti, *Cell response equalization of the ATLAS electromagnetic calorimeter without the direct knowledge of the ionization signals*, SN-ATLAS-2005-054.

[10] C. Collard et al., *Prediction of signal amplitude and shape for the ATLAS electromagnetic calorimeter*, ATL-LARG-PUB-2007-010.

[11] M. Aharrouche et al., *Response Uniformity of the ATLAS Liquid Argon Electromagnetic Calorimeter*, Nucl. Instrum. Methods A582, (2007), 429-455.

[12] I. Nikolic-Audit and L. Serin, *Time resolution of the ATLAS barrel liquid argon electromagnetic calorimeter*, ATL-LARG-2004-002.

[13] W.-M. Yao et al., *Review of Particle Physics*, J. Phys. G 33, 1 (2006).

[14] L. Gauthier, *Timing With Cosmics*, presentation given in LAr Detector and Cosmic Analysis Meeting, July 5th 2007.

Appendix 1: Comments on the Landau distribution of cosmic muons

Properties of the Landau distribution

Cosmic muons lose energy in the EM calorimeter primarily through ionization. The following formula gives the most probable energy value (MPV) of the Landau probability distribution function which describes the fluctuation in energy loss of a heavy ($m \gg m_e$) charged particle traversing through matter [13]:

$$\text{MPV} = \xi\Big[\ln\frac{2mc^2(\beta\gamma)^2}{I} + \ln\frac{\xi}{I} + j - \beta^2 - \delta(\beta\gamma)\Big], \tag{5}$$

where $\xi = (K/2) < Z/A > (x/\beta^2)$, with x representing the detector thickness in $\text{g}\cdot\text{cm}^2$. We will primarily be interested in cosmic muons with $E > 1\,\text{GeV}$ in which case $\beta \approx 1$. K is a constant with value $0.307\,\text{MeV}\cdot\text{cm}^2\cdot\text{mol}^{-1}$, Z is the atomic number of the absorber, A is the atomic mass, and $j = 0.200$. $\delta(\beta\gamma)$ is the density-effect correction to ionization energy loss and I is the mean excitation energy.

Formula 5 can also be compactified and expressed as

$$\text{MPV} = ax\Big[2\ln\beta\gamma + \ln ax + b\Big], \tag{6}$$

where x now represents the muon path length in the detector and a and b are energy and path length independent quantities (ignoring the density-effect correction). This formulation shows that the MPV scales logarithmically with energy through the dependence on γ in the first term inside the brackets (assuming $\beta \approx 1$). Second, the MPV scales with the path length as $ax(c + \ln ax)$, with $c = 2\ln\beta\gamma + b$. Furthermore it can be shown that $\ln ax \ll c$ and thus that the MPV is essentially proportional to the path length. In addition, the Landau width is also proportional to the path length [13].

Landau distribution in simulation

Both purely projective mono-energetic muons and cosmic muons have been simulated to better understand the EM calorimeter response. The simulated events were produced with GEANT 4.7 using the ATLAS detector description. With the projective muon samples (at $\eta = 0.3$) of fixed energies between 5 and 250 GeV, the dependence on energy of the Landau MPV and width have been studied. Figure 26 displays the results. As explained above, the Landau MPV scales as the logarithm of the muon energy. The energy deposition of a 5 GeV muon is 10% lower than a 250 GeV muon.

As cosmic muons have a falling energy spectrum, this dependence will effect the distribution of measured energy depositions in the calorimeter. Furthermore, the dependence may introduce a non-uniformity in η if the commissioning setup does not uniformly accept the cosmic energy spectrum. To study this effect, muons were generated at the surface according to the cosmic muon flux model and propagated to the detector if their energy at the surface was greater than 5 GeV and their distance to the interaction point less than 2.5 m. Without the access shafts shown in Figure 27a, the largest trigger rate should occur at $\eta = 0$ where the distance though the rock would be minimal (~ 62 m). These muons correspond to those located in Figure 27b

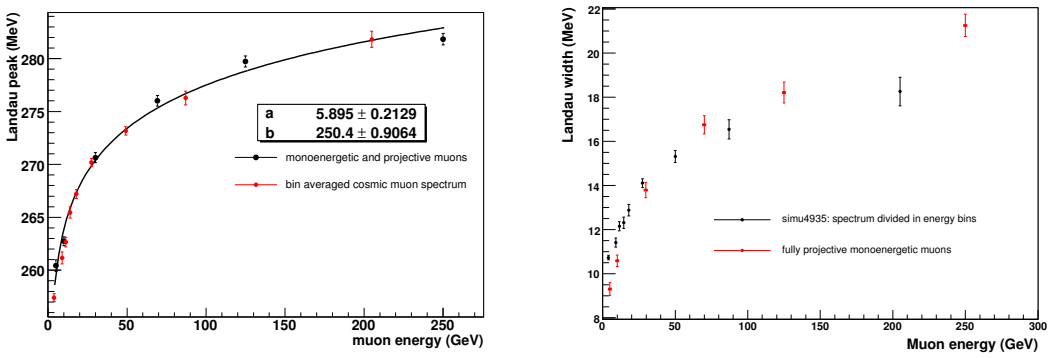

(a) (b)

Figure 26: *The MPV (left) and width (right) of the Landau distribution depend both logarithmically on the energy of the muon. The fitted parameters correspond to a function of the type* $aln(E/b)$.

above this cutoff. In order for the muons to make it to the detector, an energy at the surface above 30 GeV is required. However, the presence of the two shafts allows less energetic muons to reach the detector, and in fact represents a large fraction of the triggered events (these events are located with a distance in the rock value less than ~ 62 m in Figure 27b). The different size of the two access shafts and their position is not symmetrical with respect to the center of the detector, introducing an asymmetry in the trigger rate and in the energy spectrum of the muons at the detector.

The latter effects have been studied in the simulation. As the true energy of the muon at the entrance of the cavern was not stored in the events, an estimate has been calculated using the generated energy at the surface and an average energy loss in the rock of 0.6 GeV/m deduced from the lower limit of the distribution of the energy at the surface versus the distance traversed in the rock (Figure 27b). The reconstructed energy spectrum of trigger events at $\eta = 0.2$ through the large shaft and $\eta = -0.2$ through the small shaft are compared in Figure 28a. As expected more events are triggered in the large shaft with a softer energy spectrum. As a check of the estimate of the cosmic muon energy in the cavern, the dependance of the signal measured in the calorimeter with this energy has been studied and is in good agreement with the behavior found for mono-energetic muons (Figure 26). The asymmetry between the energy spectrum for the events triggered in each shaft introduces a small non-uniformity between positive and negative η at the level of 1-2 % and is displayed in Figure 28b.

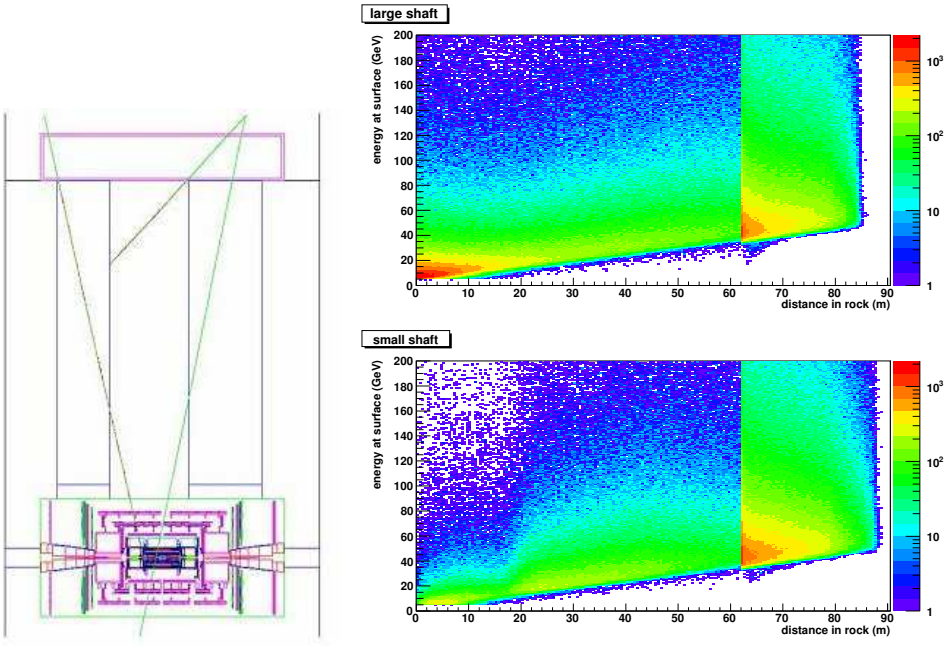

(a) (b)

Figure 27: *(a) Schematic depiction of the position of the detector relative to the access shafts and the trajectories of cosmic muons. (b) Number of triggered simulated events as a function of the energy at the surface and the distance traversed in rock. Muons with an energy less than 30 GeV must traverse a shaft to arrive at the detector.*

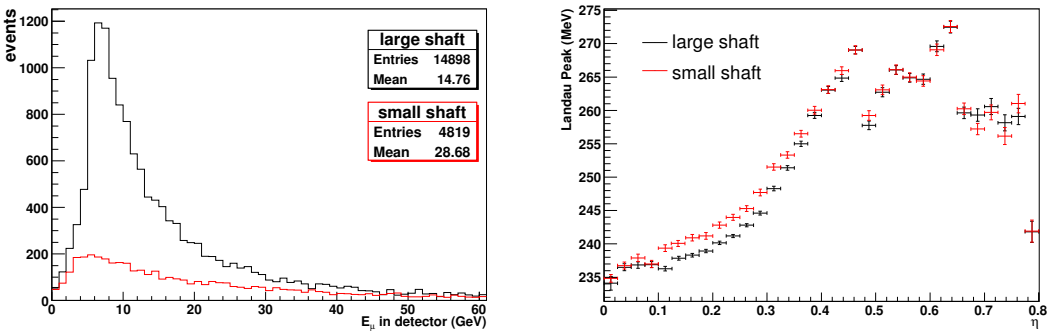

(a) (b)

Figure 28: *(a) The energy of muons at the detector separated according to the shaft traversed. (b) The response in the second sampling of the EM calorimeter as a function of* $|\eta|$ *separated according to the shaft traversed.*

Appendix 2: EM Calorimeter response as a function of applied HV

The calorimeter response as a function of the HV set (U) on the detector is proportional to U^b where b can be inferred from the simulation. This is illustrated in Figure 29 where these expectations are shown and compare with test beam data. A good agreement is observed. The simulation results are tabulated in Table 5 in the form of a factor F which is 1 for nominal (2000 V) conditions. For the note the energy reconstructed in runs taken at 1600 V are divided by 0.9190 to be added to runs taken in nominal conditions.

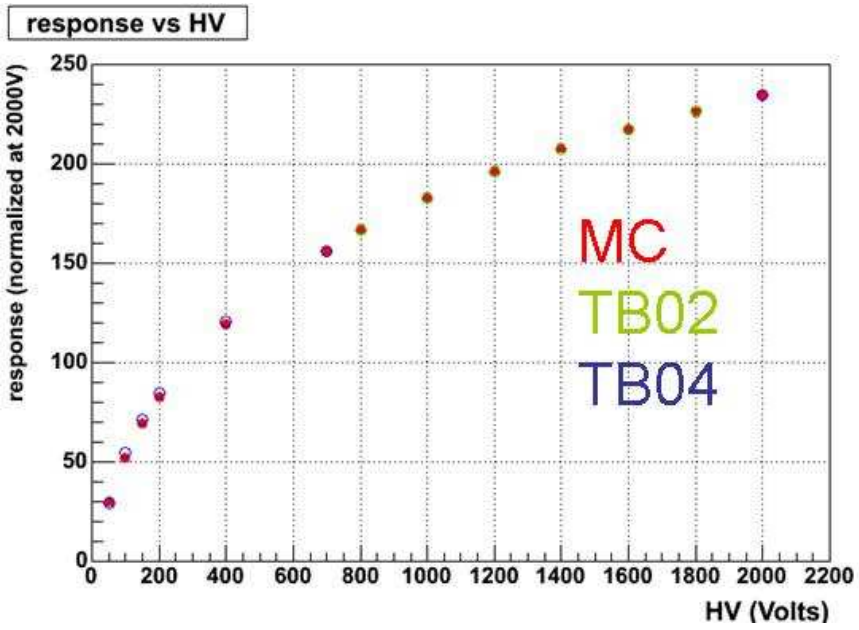

Figure 29: *Calorimeter response as a function of the HV value applied. Data from stand alone beam tests 2002 (TB02) and combined beam test 2004 (TB04) are superimpose on the simulation results.*

HV(V)	F	HV(V)	F	HV(V)	F
2000	1.	900	0.7290	300	0.4270
1800	0.9606	800	0.6906	200	0.3390
1600	0.9190	700	0.6527	150	0.2829
1400	0.8754	600	0.6065	100	0.2135
1200	0.8224	500	0.5556	50	0.1209
1000	0.7626	400	0.4961		

Table 5: Correction factor F to be applied on the reconstructed energy depending on the HV as extracted from Figure 29.